

# Semantic Correspondence: Unified Benchmarking and a Strong Baseline

Kaiyan Zhang, Xinghui Li, Jingyi Lu, Kai Han

**Abstract**—Establishing semantic correspondence is a challenging task in computer vision, aiming to match keypoints with the same semantic information across different images. Benefiting from the rapid development of deep learning, remarkable progress has been made over the past decade. However, a comprehensive review and analysis of this task remains absent. In this paper, we present the first extensive survey of semantic correspondence methods. We first propose a taxonomy to classify existing methods based on the type of their method designs. These methods are then categorized accordingly, and we provide a detailed analysis of each approach. Furthermore, we aggregate and summarize the results of methods in literature across various benchmarks into a unified comparative table, with detailed configurations to highlight performance variations. Additionally, to provide a detailed understanding on existing methods for semantic matching, we thoroughly conduct controlled experiments to analyse the effectiveness of the components of different methods. Finally, we propose a simple yet effective baseline that achieves state-of-the-art performance on multiple benchmarks, providing a solid foundation for future research in this field. We hope this survey serves as a comprehensive reference and consolidated baseline for future development. Code is publicly available at: <https://github.com/Visual-AI/Semantic-Correspondence>.

**Index Terms**—Semantic Correspondence, Semantic Matching, Image Matching, Correspondence Estimation

## I. INTRODUCTION

**S**EMANTIC matching establishes keypoint correspondences that share equivalent functional or contextual roles across different images, regardless of variations in appearance, pose, or viewing conditions. For instance, it can identify corresponding points between images such as the tips of animal ears, corners of building windows, or joints of human bodies, even when these elements exhibit different visual characteristics. Semantic correspondence facilitates various computer vision tasks: it enables structural analysis in scene understanding [1–3], ensures semantic consistency of content during style transfer [4, 5], and guides coherent manipulations in image editing [6–8]. By establishing meaningful point-to-point relationships across images, it provides essential semantic guidance for these applications. However, establishing these correspondences remains challenging, as keypoints with the same semantic information may have significantly different appearances. This requires methods to rely on high-level abstract information to find matches. Early methodologies [3, 9, 10] primarily rely on handcrafted features to establish correspondences in image pairs. However, these are fragile when faced with large appearance variations. More

recently, learned features have become prominent, allowing semantic correspondence to achieve significant progress in recent years. Recent approaches [11–16] rely on deep convolutional neural networks (CNNs) to extract semantic features. A wide range of network architectures and paradigms have been explored, ranging from CNN architectures [17–20] to transformer modules [21–23]. More recently, vision foundation models, such as DINOv2 [24] and Stable Diffusion [25], have demonstrated remarkable zero-shot semantic correspondence capability [26, 27], enabling follow-up works [28–30] to achieve state-of-the-art performance.

Semantic matching is a relatively new and distinct task in computer vision, standing apart from established tasks such as geometry matching, stereo matching, and optical flow estimation. Geometry matching [31, 32] primarily involves identifying correspondences between points representing the same physical location across images. It heavily relies on spatial consistency, often constrained by the spatial arrangement of the scene. Stereo matching [33], on the other hand, estimates depth by matching corresponding pixels in rectified stereo images, leveraging the constraints of epipolar geometry. In contrast, optical flow estimation [34] emphasizes the motion of pixels or objects between consecutive frames in a video sequence to capture temporal dynamics. Unlike these tasks, semantic correspondence focuses on aligning semantically similar regions or objects across images, without being constrained by spatial and geometric constraints. This task is unique in its objectives, methodologies, and application scenario. Therefore, in this paper, we focus primarily on the unique challenges and advances of semantic matching.

Since the study of semantic matching has evolved significantly, it is critical to track the literature; categorize and analyze existing methods; and reflect on their progress. Figure 1 presents a summarized timeline of the development of semantic matching methods, highlighting the rapid progress in this field. The diversity and sheer number of emerging methods make it challenging to discern their relationships and developmental trajectories. Furthermore, the fragmented nature of existing literature hinders the researcher’s understanding of the overall impact of these methods on the task, let alone grasp their differences and innovations. To address this challenge, we propose a taxonomy to classify existing methods based on their general designs, dividing them into three main categories: early attempts, architectural improvements and training strategy improvements, as shown in Figure 2. Early attempts primarily tackle this task using handcrafted feature such as SIFT [35] or HOG [10]. Architectural improvements focus on enhancing representation learning and matching quality, while

Kaiyan Zhang, Jingyi Lu, and Kai Han are with The University of Hong Kong.

Corresponding author: Kai Han (kaihanx@hku.hk)

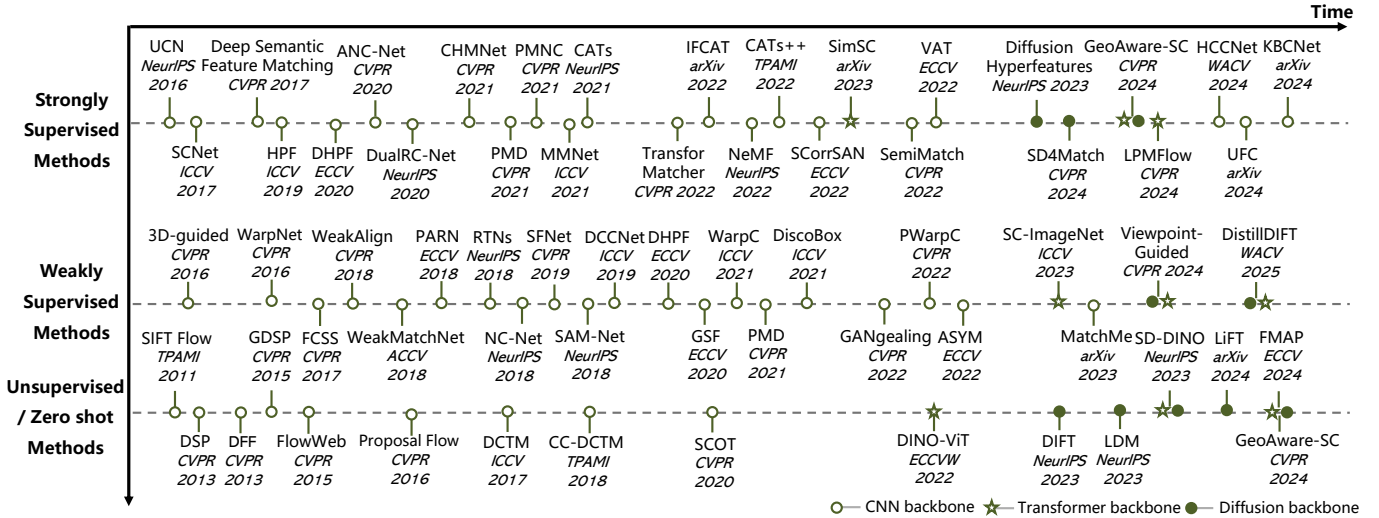


Fig. 1. **The development timeline of semantic correspondence methods categorized by their levels of supervision.** These categories include strongly supervised, weakly supervised, and zero-shot methods. Each method is labeled with its backbone architecture, indicated by distinct symbols:  $\circ$  for CNN backbones,  $\star$  for vision transformer backbones, and  $\bullet$  for stable diffusion backbones. For methods that utilize both vision transformer backbones and stable diffusion backbones (e.g., DINOv2+SD), we use a combination of a  $\star$  and a  $\bullet$  to represent their hybrid architecture.

training strategies aim to improve the matching performance by optimizing how the model learns. This taxonomy provides a structured framework for systematically analyzing and comparing different methods. It enables researchers to quickly identify the position and contributions of each approach within the field and supports the establishment of unified benchmarking for consistent evaluation.

Existing methods exhibit differences in backbone type, fine-tuning strategy, and model architecture, yet a unified evaluation remains absent. This inconsistency hinders objective comparisons, making it difficult to isolate the impact of specific components. To address this, we conduct extensive experiments across these factors and reveal that fine-tuning a powerful backbone is the most decisive factor affecting performance. Building on this finding, we propose a benchmark to enable more objective and transparent comparisons.

Based on our benchmarking and analysis, we integrate the most effective components from each stage of semantic correspondence methods to propose a simple yet strong baseline. This baseline achieves state-of-the-art performance across multiple public benchmarks, providing a strong foundation for future development.

In summary, we make the following contributions:

- We propose a clear taxonomy and provide a comprehensive survey for existing semantic correspondence methods, categorizing them based on their general design and summarizing their key contributions.
- We systematically conduct extensive experiments to evaluate the performance of existing methods across various benchmarks, providing insights into their strengths and weaknesses.
- We propose a simple yet effective baseline that achieves state-of-the-art performance on multiple benchmarks, offering a strong foundation for future research in this field.

## II. PROBLEM STATEMENT

Given a pair of source and target images,  $I^s$  and  $I^t$ , and a set of query points  $\mathbf{X}^s = \{\mathbf{x}_q^s = (x_q^s, y_q^s) \mid q = 1, 2, \dots, n\}$  in  $I^s$ , semantic matching aims to find corresponding points  $\bar{\mathbf{X}}^t = \{\bar{\mathbf{x}}_q^t = (\bar{x}_q^t, \bar{y}_q^t) \mid q = 1, 2, \dots, n\}$  in  $I^t$  that share the same semantic meaning as those in  $\mathbf{X}^s$ .

Semantic matching methods can be broadly divided into sparse and dense correspondence, depending on the number of matched points. Sparse methods estimate correspondences for a few query points, while dense methods aim to predict correspondences for all pixels. A widely adopted pipeline for semantic correspondence involves extracting feature vectors  $\{f_q^s \in \mathbb{R}^c \mid q = 1, 2, \dots, n\}$  for the query points  $\mathbf{X}^s$ , and a dense feature map  $F^t \in \mathbb{R}^{H_t \times W_t \times C}$  for the target image  $I^t$ , using a feature extractor  $f(\cdot)$ . Each query feature  $f_q^s$  is then compared to all locations in  $F^t$ , and the most similar feature  $\bar{f}_q^t$  is identified. The spatial location of  $\bar{f}_q^t$  within  $F^t$  is taken as the predicted correspondence.

The most crucial component in this pipeline is the feature extractor  $f(\cdot)$ , as it forms the foundation for accurate matching. Consequently, designing a discriminative and generalizable feature extractor has become a central research focus in this domain. In addition, the inference stage—beyond simply selecting the most similar feature—can also be improved using more sophisticated algorithms, representing another active research direction.

In the following sections, we present our taxonomy of existing literature and provide a detailed review of each method.

## III. METHOD REVIEW

### A. Overview

To provide a structured understanding of semantic correspondence methods, we present a taxonomy categorizing

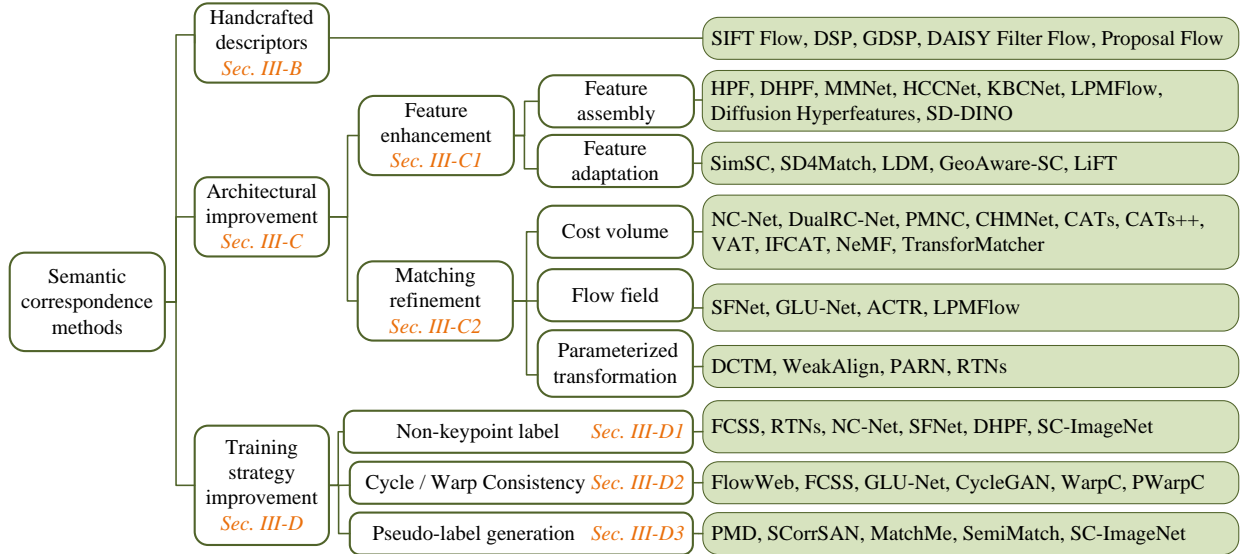


Fig. 2. **Taxonomy of semantic correspondence methods.** This taxonomy provides a comprehensive overview of the diverse approaches to enhance feature quality, matching performance, or training strategies. Only a few representative methods of each category are shown.

approaches into handcrafted descriptors, architectural improvements, and training strategy improvements, as shown in Figure 2. This taxonomy traces the evolution from handcrafted methods to advanced deep learning solutions, providing a clear overview of how different approaches enhance feature quality, matching performance, and training strategies.

### B. Handcrafted Descriptors

Early methods establish semantic correspondence by matching two sets of local regions based on handcrafted feature descriptors.

For example, Scale-Invariant Feature Transform (SIFT) [35] and Histograms of Oriented Gradients (HOG) [10] are widely used to extract local features from images. Lazebnik *et al.* [36] utilized SIFT to represent local regions (keypoints) in images, capturing features that may correspond to textures or object components. Building on this, Kushal *et al.* [37] demonstrated that SIFT could also be leveraged to compute appearance-based primary matches between salient image regions. Through circular region detection using the Hough Transform and SIFT feature extraction, they calculated the similarity between these regions by comparing their SIFT descriptors. Furthermore, SIFT Flow [3], inspired by classic optical flow algorithms, extends the application of SIFT descriptors to dense pixel-level matching, emphasizing the semantic coherence of the entire image rather than focusing solely on local salient region matching. Kim *et al.* [38] further enhanced this approach by inducing a multi-scale regularization with a hierarchically connected pyramid of grid graphs. Yang *et al.* [39] employed DAISY [40] descriptors to handle non-rigid geometric transformations. Meanwhile, Cho *et al.* [9] proposed a voting-based algorithm that utilizes region proposals and HOG [10] features for semantic matching and object discovery. Ham *et al.* [41, 42] also utilized HOG features extracted from object proposals to establish region correspondences.

These techniques typically focus on matching features from handcrafted descriptors, such as SIFT [3, 38, 43, 44], DAISY [39] and HOG [45–48]. Additionally, other approaches have been explored, such as graph-based matching algorithms [49, 50], which leverage flexible graph representations to find category-level feature matches, and probabilistic matching algorithms [9, 45, 46], which model uncertainty in feature correspondences using probabilistic frameworks. But they often struggle with large appearance or viewpoint changes, which limits their robustness in more challenging scenarios.

With the rise of deep learning, research has moved from handcrafted to learned features, improving reliability and enabling more flexible, scalable solutions for semantic matching. In this work, we focus on learning-based approaches, which have shown notable effectiveness in addressing these challenges.

### C. Architectural Improvements

Backbones trained on large-scale datasets have shown strong general-purpose feature extraction capabilities. Consequently, research in this field has increasingly shifted toward how to effectively leverage learned features by innovation in the architecture of the overall pipeline.

Generally, the literature in architectural improvements can be divided into two families: feature enhancement and matching refinement. The former focuses on extracting more discriminative features and could be further categorized into two sub-families: feature assembly and feature adaptation; while the latter aims to refine matches established by feature maps and can be categorized into three classes: cost volume, flow field, and parameterized transformation based matching refinement. In the following paragraphs, we first introduce feature enhancement and its two sub-families in Section III-C1, followed by the review of three matching refinement classes in Section III-C2.

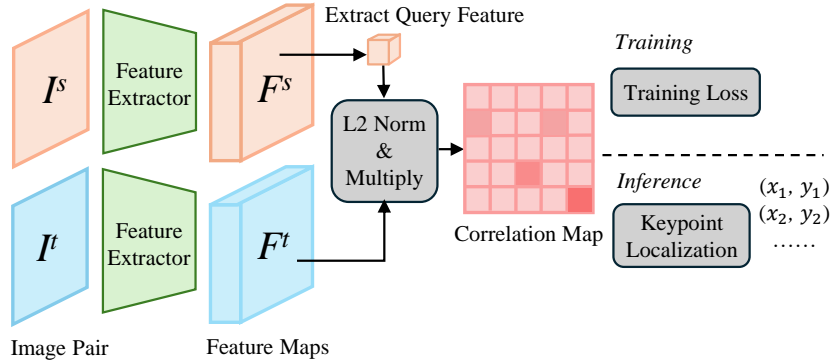


Fig. 3. **Pipeline for feature enhancement methods.** The feature extractor generates feature maps  $F^s$  and  $F^t$  from the source image  $I^s$  and target image  $I^t$ , respectively. After channel-wise L2 normalization, their dot product constructs a cosine similarity matrix (2D correlation map) for each query point in  $F^s$ . The correlation map is transformed into a probability distribution through a localization operation such as soft-argmax, which is then supervised by a ground-truth distribution derived from ground-truth correspondences using the same localization technique. During inference, the correlation map localizes the correspondences  $(x_1, y_1), (x_2, y_2), \dots$  in  $I^t$ .

1) *Feature Enhancement*: Early deep learning methods typically learned features from scratch. For instance, Choy *et al.* [51] developed a similarity metric using a contrastive loss combined with hard negative mining; Han *et al.* [11] proposed a scoring function using a CNN to rank the similarity between patches identified by region proposals and determined correspondences through probabilistic Hough matching [10]; Kim *et al.* [12] introduced a CNN self-similarity feature, which is utilized to estimate dense affine transformation fields. While these approaches showcase promising results, their performance and generalizability are constrained by the limited scale of training data.

Long *et al.* [52] have shown that CNNs pre-trained on image classification tasks could extract features for semantic correspondence without additional training. The capability to perform matching without task-specific fine-tuning in some cases highlights the strength of object information learned from millions of images. This suggests that, instead of training semantic features from scratch, one could develop a more accurate and generalizable matching pipeline by leveraging pre-trained CNNs. Such a pipeline takes a straightforward architecture: a dense feature map is first extracted from the input image and the correlation map between query and candidate features is computed. This correlation map is then transformed into correspondences using keypoint localization techniques such as argmax or kernel soft-argmax operations [1]. We illustrate this pipeline in Figure 3.

A key component in the pipeline is the feature extractor, as it significantly affects the subsequent correlation map and the accuracy of the final correspondence. While a pre-trained CNN, as shown by [52], can fulfill this purpose, it can be further enhanced to yield more powerful feature extractors. Two commonly used strategies in the literature for improving feature extraction are *feature assembly* and *feature adaptation*. Feature assembly constructs hyper-features by combining multiple complementary features [13, 16, 27, 53–57], while feature adaptation employs an adaptation module to transfer pre-trained features to the semantic matching task [28, 29, 58–60]. We review both strategies in the following paragraphs. It is worth noting that more recent methods [26, 27, 29, 57] switch from CNN backbones to more powerful counterparts such

as diffusion models [25] or DINOv2 [24] and significantly improve accuracy. The general ideas behind these methods fall into our categorization. Our review is not tied to a specific backbone family but approaches from the perspective of methodology.

**Feature Assembly.** Semantic matching finds correspondences by overcoming appearance differences brought by intra-category variation and pose changes. A good feature should contain both abstract information—such as high-level semantic priors that encode object structured and functional part relationships—and local details to accurately localize the correspondence. Consequently, one line of work focuses on assembly features from different layers of CNN to produce a hyper-feature that includes different levels of information about the scene.

Hariharan *et al.* [53] showed that combining features from multiple layers of CNN into a “hypercolumn” significantly improves feature’s performance in object detection, segmentation, and part labeling. Inspired by this, Min *et al.* [13] introduced “hyperpixels”, which leverages different levels of features from early to late layers of CNN with beam search [61], enabling the disambiguation of image parts across multiple visual aspects. Further extending this idea, dynamic hyperpixel flow (DHF) [14] was developed to dynamically compose hypercolumn features by selecting a small number of relevant layers from CNN. By leveraging these relevant layers, conditioned on the specific images to be matched, DHF [14] composes effective features on the fly, and the resultant hyperpixels provide both fine-grained and context-aware features, making DHF a powerful approach for feature assembly. Unlike “hypercolumns” and “hyperpixels”, which are obtained by searching or selecting features from various layers, MMNet [54] fuses feature maps from all residual blocks within the same group. In contrast to FPN [62], which only utilizes the feature map of the last residual block in each convolutional group, MMNet [54] captures semantics at different levels. Kim *et al.* [16] proposed a technique called “feature slicing” to generate richer multi-scale correlation maps by slicing intermediate feature maps into smaller, equi-channel segments, which maximize the potential of the constructed hypercolumn correlation. These multi-scale correlation maps

are then concatenated along the channel dimension to obtain a hypercolumn correlation. Jin *et al.* [55] proposed the Key-point Bounding box-centered Cropping (KBC) method. This approach involves digitally unsampling the source image to increase the separation of closed keypoints on small objects if necessary, and then cropping it to match the input size based on the keypoint bounding box. This technique facilitates the independent learning of these keypoints. KBCNet [55] applies cross-attention to leverage fine-grained and deep semantic features across scales within the same image, thereby enhancing the robustness and accuracy of semantic correspondence. LPMFlow [56] progressively generates feature maps at different scales by employing self-attention and cross-attention mechanisms to enhance and upsample features, producing hybrid enhanced features that incorporate both self-feature guidance and interaction-enhanced super-resolution features, aiming to obtain detailed semantic representations while increasing feature resolution.

More recently, features of large foundation models, such as diffusion models [25, 26] and DINOv2 [24], have better performance over those of CNN backbones due to larger training data and attention. This encourages research [27, 29, 57] in adopting the idea of feature assembly to foundational models. For instance, Luo *et al.* [57] proposed to concatenate all intermediate feature maps from the diffusion model, across different network layers and diffusion timesteps, into a single per-pixel descriptor for semantic correspondence. Similarly, Zhang *et al.* [27] observed that features from stable diffusion (SD) exhibit complementary properties to those from DINOv2. Therefore, by combining them into a single feature, they achieve stronger zero-shot performance.

Although feature assembly achieves good results by constructing “hyper-features”, the dimension may be very large, which increases the memory consumption and slows down the pipeline. An alternative is to select a specific layer feature and adapt it to the matching task, which keeps the dimension of the feature relatively low, accelerating matching. We review this line of work in the next paragraphs.

**Feature Adaptation.** Unlike feature assembly, feature adaptation improves the quality of features by adapting them to the semantic matching task. It can be achieved by appending a trainable adaptation module or fine-tuning the feature backbone using matching loss. SimSC [58] introduces a generic and simple learning pipeline to fine-tune backbones using adaptive temperature learning. It employed a lightweight temperature learning module to find the optimal temperature for the softmax operation to alleviate the gradient suppression caused by L2 normalization during training. Building on top of it, SD4Match [28] explores how to optimize the prompt to enhance the performance of Stable Diffusion’s feature [26] in semantic correspondence, and introduces a conditional prompting module to infuse prior knowledge of objects to the diffusion model, increasing the quality of the feature. LDM [59] leverages Stable Diffusion for semantic matching from a different perspective. It borrows the idea of textual inversion [63] and learns an embedding for a query point in the source image. Such an embedding is transferred to the target image to locate the correspondence from the attention map

of the target image with the embedding. GeoAware-SC [29] employs SD-DINO [27] as the feature backbone and uses a CNN to adapt the feature to the semantic matching task. Additionally, it improved the geometry-aware ability of the model by data augmentation. LiFT [60] introduces a post-processing method to replace the naive bilinear interpolation when upsampling the ViT feature for better performance. Starting from a low-resolution ViT feature, it learns to reconstruct the high-resolution ViT feature in a self-supervised manner.

Compared with other methods, feature adaptation is an efficient pipeline as the network focuses solely on extracting features from images. However, the model is prone to overfit the training dataset, showing inferior generalizability.

We have reviewed feature enhancement, which primarily focuses on improving features extracted from the images. The second family of work, matching refinement, aims to refine the initial matches established from the feature backbone. We will review this topic in the next section.

2) *Matching Refinement:* After obtaining feature maps, matches can be established by comparing the features of the source image with those of the target image. The most intuitive approach is to compute the similarity between each pair of features and select the best match. Several keypoint localization techniques have been explored:

- **Nearest Neighbor (NN)** [17, 26, 27, 64–67]: For each feature in the source image, it finds the feature in the target image with the highest similarity score through direct comparison of feature vectors.
- **Bilinear Interpolation** [1, 2, 23, 56, 58, 59, 68–72]: It computes the correspondence by taking weighted combinations of neighboring features, where the weights are determined by the relative position of the query point to its neighbors in a regular grid.
- **Kernel Soft Argmax** [1, 2, 16, 19, 21, 58, 73–75]: This method extends Soft Argmax by using kernel function to convert feature distance into similarity. In general, similarity score  $s_i$  is first converted into probability by softmax:  $p_i = \frac{\exp(s_i)}{\sum_j \exp(s_j)}$ , then compute the expected coordinate as  $\sum_i p_i \cdot c_i$ , where  $c_i$  is the coordinate value. For example, with a Gaussian kernel, the similarity is computed as  $\exp(-\|f_1 - f_2\|^2/\sigma^2)$ , where  $f_1$  and  $f_2$  are feature vectors and  $\sigma$  controls the kernel width.
- **Window Soft Argmax** [29, 30, 76, 77]: For each feature point, this method defines a  $k \times k$  window centered at that point. The matching score at position  $(x, y)$  is computed as the weighted sum of similarities within this window:  $\sum_{i,j \in W} w_{ij} \cdot s(f_{x+i, y+j})$ , where  $W$  is the window region,  $w_{ij}$  is spatial weight, and  $s(\cdot)$  is the similarity function.

However, these methods heavily rely on the quality of the feature map and consider each matching individually. They are prone to outliers and noise in the feature map.

To address this issue, match refinement has been explored to consider the matching globally. Intuitively, good matches should be spatially continuous, smooth and follows certain patterns, rather than being stochastic with abrupt change. This indicates that teaching the model to recognize and correct unreliable matches could also improve the matching accu-

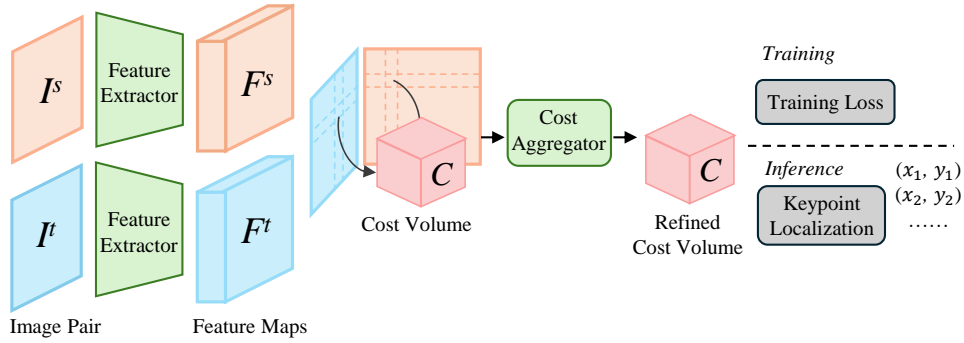


Fig. 4. **Pipeline for cost volume-based methods.** The feature extractor generates feature maps  $F^s$  and  $F^t$  from the source image  $I^s$  and target image  $I^t$ , respectively. After normalization, their dot product constructs a cost volume for each query point in  $F^s$ , storing the cosine similarity between all possible feature pairs. This cost volume is refined by a cost aggregator and converted into a probability distribution via softmax, supervised by a ground-truth distribution derived from known correspondences. During inference, the correlation map localizes the correspondences  $(x_1, y_1)$ ,  $(x_2, y_2)$ ,  $\dots$  in  $I^t$ .

racy. Generally, there are three common formats for matches: cost volume [17, 18, 20, 23, 78], flow field [1, 2, 56, 72] and parameterized transformation [79, 80]. Cost volume is a high dimensional tensor storing the likelihood of all possible matches between two images; flow field is a 2D vector field indicating the correspondence for each spatial position; and parameterized transformation represents matches as the wrapping between two images using few parameters. The majority of the literature in this direction refines matches based on these three formats. We review methods on each format in the following paragraphs.

**Cost Volume.** The cost volume, also known as the correlation tensor, is a high dimensional tensor that stores the similarities between all possible feature pairs between two images. Given two image feature maps  $F_s \in \mathbb{R}^{H_s \times W_s \times C}$  and  $F_t \in \mathbb{R}^{H_t \times W_t \times C}$ , the cost volume is normally expressed as a 4D tensor  $C \in \mathbb{R}^{H_s \times W_s \times H_t \times W_t}$  or a 2D matrix  $C \in \mathbb{R}^{H_s W_s \times H_t W_t}$ . The simplest way to find the correspondence is by slicing the cost volume at the position of the query point and applying the argmax operation. With a perfect feature extractor, this is good enough to localize accurate correspondence. However, the real feature extractor could be mistaken by the ambiguity or noise within images, leading to incorrect correspondences after the argmax operation. Apart from features, matching patterns provide valuable information as well. Intuitively, good dense matching should be smooth, and continuous without abrupt changes. This provides extra constraints on matching, offering an alternative perspective to feature enhancement methods and complementary insights into the matching problem. Based on this intuition, the cost volume-based methods apply a learnable cost aggregation module to the cost volume and refines it by recognizing the correct matching pattern. Figure 4 illustrates the general pipeline of this line of work.

One of the most powerful constraints is the neighborhood consensus constraint, which assumes that correspondences of adjacent query points should follow a similar local pattern to the query points. It has been widely used in geometric matching to filter outliers [81–84]. In the context of semantic correspondence, the seminal work in exploring the neighborhood consensus constraint is NC-Net [17]. It employs a 4D convolutional module, consisting of a series of  $5 \times 5 \times 5 \times 5$  convolutional kernels, and applies it to the

cost volume to recognize reliable matches from local matching patterns, showing good results. It inspired a line of follow-up works exploring the cost volume for semantic matching: ANC-Net [18] proposes an adaptive neighborhood consensus module that contains a set of non-isotropic 4D convolutional layers, such as kernels with the size of  $3 \times 3 \times 5 \times 5$ , enabling the model to handle the scale difference between objects. DualRC-Net [70, 71] follows the idea of ANC-Net, and proposes a learning mechanism to dynamically combine different non-isotropic 4D kernels, avoiding manually searching for the optimal weights for combination. CHM [19, 78] tackles the scale issue by incorporating scale difference into the cost volume. In addition to two spatial dimensions height and width, an extra dimension of scale upgrades the cost volume to 6D. By employing a 6D convolutional module, the method performs position-aware Hough voting in the high-dimensional space, improving the matching accuracy. MMNet [54] builds the final cost volume by incorporating information from intermediate features and cost volumes. GSF [73] first employs a learnable pruning module to select reliable initial matches from the cost volume and uses selected matches as the anchor point and refines neighbouring matching scores using the Gaussian process. PMNC [20], instead of processing the full cost volume, predicts the matching score of a specific correspondence pair by taking the local cost volume centered at the pair and iteratively refining the initial matches using the PatchMatch [85] algorithm. As it only processes a fraction of the cost volume at a time, this method is significantly faster than the aforementioned methods. Although the neighborhood consensus constraint by high-dimensional convolution is effective in recognizing correct matches, it focus on locality limits the ability to capture global matching patterns. This has motivated a shift towards transformer architecture, which enables direct modeling of long-range dependencies and global matching patterns in the correspondence space.

Transformer network architecture [86] has demonstrated remarkable capability across a wide range of computer vision tasks [87–90]. The success is attributed to the global dependency between features realized by the attention mechanism. CATs [21] is the first to employ a transformer module to do cost aggregation, aiming to overcome the limitations of CNNs’ local receptive fields through the global self-attention mechanism of this architecture, thereby demonstrating the

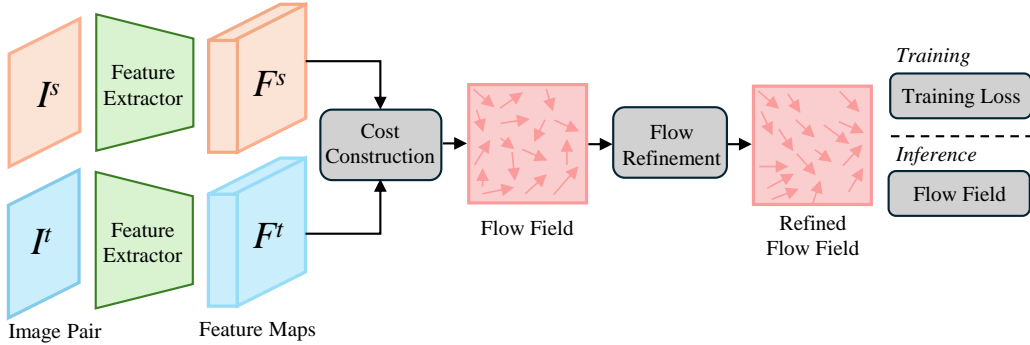


Fig. 5. **Pipeline for flow field-based methods.** Given a pair of images  $I^s$  and  $I^t$ , feature extraction is performed to obtain dense feature maps  $F^s$  and  $F^t$  respectively. The cost construction step is then applied to derive a cost volume, which is subsequently transformed into a flow field. The flow field represents the correspondence between each pixel in the target image and its corresponding pixel in the source image.

feasibility of the transformer as a cost aggregator. Specifically, CATs transforms the cost volume into token sequence and incorporates positional embeddings to retain spatial information. The tokenized sequence is then processed by a standard transformer module, which performs global aggregation and optimization of the matching scores, producing a refined cost volume. CATs++ [22] extends CATs [21] by introducing early convolutions before the transformer cost aggregator. By leveraging both convolution and transformer, it combines the strengths of both techniques and enhances the model’s ability through local interactions before globally aggregating pairwise interactions. VAT [91] introduces a 4D Convolutional Swin Transformer, which consists of a high-dimensional Swin Transformer [92] preceded by a series of small-kernel convolutions. This alleviates the local context loss caused by the tokenization of the transformer, improving the capture of local features and overall performance. Similarly, NeMF [93] tackles the local context loss by integrating the transformer architecture with convolutional operators. This approach allows for the local and global integration of matching cues by encapsulating local contexts and imparting them to all pixels via self-attention. In addition to aggregation on the cost volume, IFCAT [68] employs a similar aggregation module directly on the feature space, leveraging their complementarity. The aggregation in the feature space helps disambiguate the noise in the cost volume, while the cost volume enhances feature aggregation by introducing matching similarities as a factor for aggregation. TransforMatcher [23], unlike previous methods that reshape the 4D cost volume into 2D for patch-to-patch attention, treats every match on the correlation map as an input element. It uses multi-level scores as features to perform match-to-match attention, enabling more fine-grained interactions.

Transformer cost aggregation methods have introduced a new paradigm to semantic correspondence by leveraging the attention mechanisms of the transformer. Despite the effectiveness of the global self-attention mechanism in integrating global information, computational efficiency becomes a drawback when processing high-resolution images. Additionally, due to the data-hungry nature of the transformer architecture, these methods require extensive data augmentation to improve generalizability.

**Flow Field.** In addition to representing the dense matching between two images as a cost volume, a common alternative

is the flow field. A flow field is a 2D vector field  $M \in R^{H_s \times W_s \times 2}$  where each spatial location records the offset to its correspondence in the target image. The flow field facilitates precise semantic matching by providing an accurate and continuous mapping of pixel-level correspondences. Similar to the cost volume-based methods, the flow field-based method employs a flow refinement module, learning to refine the initial flow field based on various types of constraints, such as smoothness or the neighbourhood consensus. An abstract illustration of this line of work is in Figure 5.

Several methods have been explored in this direction. Proposal flow [41, 42] first introduces object proposals to establishing region correspondence. It generates semantic flow between similar images by leveraging both local and geometric consistency constraints among object proposals and demonstrates that proposal flow can effectively be transformed into a dense flow field. SFNet [1] proposes using binary foreground masks as a supervisory signal to establish object-aware semantic flow. By incorporating mask-flow consistency and smoothness terms, SFNet is trained end-to-end to establish object-aware correspondences while filtering distracting details. GLU-Net [65] integrates global and local correlation layers to effectively manage both large and small displacements. The network processes low-resolution images for global correlation, capturing long-range correspondences, and then refines the flow estimation on high-resolution images through local correlations. ACTR [72] fuses the multi-path coarse flows for refinement to benefit from different matching tensors. LPMFlow [56] refines flow estimation by integrating multi-scale matching flows. Specifically, flows are progressively refined using Swin-attention across various window sizes, enabling the final high-resolution flow to accurately capture fine local details, thereby incorporating correspondence in different ranges to distinguish subtle differences in narrowed pixel regions.

Due to the similarity between cost aggregation methods, flow field-based methods generally adopt similar network meta-architectures, such as multi-scale exploration and feature fusion, integrating information across scales and domains to enhance the accuracy of semantic correspondence.

**Parameterized Transformation.** Apart from cost volume and flow field, a third option is to represent the dense matching as the global warping between two images using transformation model, such as affine, homography, or thin-plate spline etc.

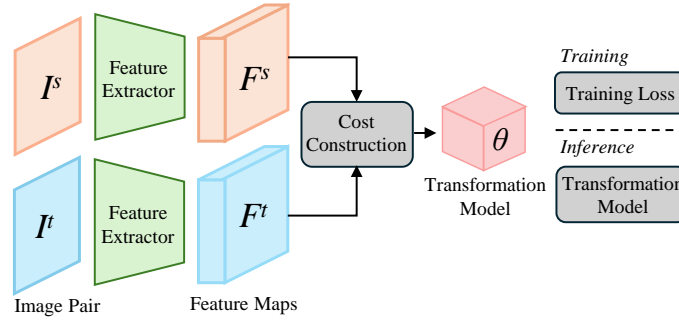


Fig. 6. **Pipeline for parameterized transformation-based methods.** Given a pair of images  $I^s$  and  $I^t$ , feature extraction is performed to obtain dense feature maps  $F^s$  and  $F^t$  respectively. The cost construction step is then applied to derive a cost volume, which is subsequently used to infer and regress the transformation parameters.

The benefit of using the transformation model is that it may automatically filter outliers during the model regression process, as resultant transformation is intrinsically smooth and continuous. Figure 6 illustrates the general pipeline of this approach.

One representative work in this direction is CNNGeo [94]. It regresses the transformation between images using geometric models such as an affine and thin plate spline (TPS) transformation through a CNN, mimicking the traditional matching pipeline. Once obtaining the parameters of the transformation, the correspondence of a query point can be directly established by applying the transformation to that point. Seo *et al.* [95] improved this approach using offset-aware correlation kernels to put more attention to reliable matches to reduce the influence of outliers when regressing the transformation. WeakAlign [79] extends this approach by proposing a weakly-supervised training method without using the ground-truth label. In addition, it proposes a soft inlier-scoring module to reduce the influence of the background cluster when estimating the transformation between objects.

Unlike previous methods where the transformation between two images is summarized by one set of parameters, DCTM [80] employs an affine transformation field, where each pixel has its own affine transformation, to describe the relationship between two images, greatly improving the flexibility of the model on the non-rigid deformation. It then alternatively optimizes the parameters on discrete and continuous space. RTN [96] follows a similar suit, but chooses to use a recurrent neural network to gradually refine the transformation field. PARN [97] constructs a network in a hierarchical nature. The bottom layer regresses one set of parameters for the global transformation between images. Going deeper down the network, each layer estimates a transformation field with a finer scale and the pixel-level transformation field is estimated in the last layer of the network. This allows the model to refine the field in a coarse-to-fine manner.

The smooth and continuous nature of the geometric transformation model enables high-quality object warping if the parameters are accurately estimated. However, these methods are easily distracted by background clutter and occlusion, as the regression of the transformation depends on correlations between feature pairs. Noise and outliers could lead to sub-optimal parameter regression, which leads to inaccurate matching on a global scale. The smooth and continuous nature

amplifies the error in this case. Although this can be alleviated by using the attention module [95] or suppressing outlier matches [79], the problem still persists.

#### D. Training Strategy

Apart from innovations in the neural network architecture, the other research direction is on the training strategy. The most convenient way to train a semantic matcher is supervised training: the model is trained with ground-truth correspondence labels between two images. However, unlike the geometric matching [60, 70, 90, 98, 99], where the dense correspondence labels can be easily obtained through multiview geometry, the correspondence labels of the semantic matching rely on manual efforts. Despite several semantic matching datasets having been released, the scale of the data and the density of the labels remain relatively small and little. This hinders the learning of an accurate and generalizable semantic matcher.

This prompts the research to reduce the training’s reliance on ground-truth keypoint labels. This line of work can be categorized into three classes: non-keypoint-based methods, consistency-based methods, and pseudo-label generation-based methods. Non keypoint-based methods explore training the model with non-keypoint labels, such as segmentation masks or images themselves, etc; consistency-based methods leverage the warping consistency between images to supervise the training and pseudo-label generation-based methods generate pseudo labels based on existing sparse labels. We introduce each family of methods in the following paragraphs.

1) *Non-Keypoint Label*: An intuitive way to address the reliance on keypoint labels is to use non-keypoint labels to train models. Several options have been explored. Object proposals are originally developed for object detection, where they help reduce the search space and minimize false alarms. Proposal flow [41, 42] first introduces object proposals to generate semantic flow between similar images. By leveraging multi-scale object proposals, it establishes region correspondences, focusing on prominent objects and parts while suppressing background clutter and distracting scene components. The Fully Convolutional Self-Similarity (FCSS) [12] introduces a weakly-supervised learning approach that incorporates object location priors, such as an object bounding box containing the target object to be matched. By this, the FCSS descriptor can be trained effectively without the need for extensive keypoint

annotations. NC-Net [17] and Dynamic Hyperpixel Flow [14] employs image-level supervision. They maximize the sum of cost volume between image pairs of the same object category and minimize that between those of different categories, implicitly encouraging the network to learn correspondences by distinguishing different objects. SC-ImageNet [100] uses categories information of the large-scale ImageNet ILSVRC dataset [101] for weak supervision. It formulates a contrastive learning task to enhance the distinction between refined cost volumes with and without matching relationships. RTNs [96] introduces a weakly-supervised classification loss to estimate the geometric transformations, based on the principle that the correct transformation for a pixel should maximize the similarity of the source features and transformed target features at that pixel, while other transformations within the search window are treated as negative examples. SFNet [1, 2] trains a CNN using images with binary foreground masks and synthetic geometric deformations, leveraging high-quality correspondences to segment matched objects. The binary masks serve as strong object-level priors, enabling object-aware correspondence learning without pixel-level ground truth.

These non-keypoint label-based methods employ various forms of supervision, such as object bounding boxes, image pairs, class labels, and binary masks, to guide the learning process. This approach enables effective learning of semantic correspondences while significantly reducing the reliance on costly manual annotations. However, most of these methods primarily use image-level loss functions that lack explicit pixel-wise or localized supervision. This coarse-grained optimization objective sometimes leads the model to converge to suboptimal local minima. Therefore, more advanced methods are needed to address these limitations, such as those based on consistency constraints.

2) *Cycle / Warp Consistency*: Cycle consistency in image matching refers to the concept that if a pixel from image A undergoes a series of correspondence matching through multiple images and eventually returns to its source image, all the matching in this process should form a closed loop and the query point will eventually return to its original position. This concept has been adopted by various semantic correspondence methods to train models without explicit keypoint label supervision.

FlowWeb [102] models an image collection as a fully connected graph, where nodes represent images and edges denote pairwise correspondence flow fields. By enforcing cycle consistency across all edges, it ensures that the cumulative displacement along any closed loop is zero, establishing globally consistent dense correspondences. FCSS [12] enforces correspondence between a source image and a target image by verifying that the matching relationship remains consistent when reversed.

Laskar *et al.* [103] adopted a similar approach, formulating the semantic correspondence task as a 2D point set registration problem. By enforcing cycle consistency in both forward and backward transformations, they ensured that keypoints from the source image, when projected onto the target image and back, return to their original positions. Similarly, Chen *et al.* [104] introduced forward-backward consistency as a loss

function, enforcing consistency by minimizing the discrepancy between the forward and backward transformation paths. Shtedritski *et al.* [105] combined ViT-DINO with cycle consistency to derive complementary learning signals, distilling a high-quality point matcher. This integration leverages the generalization ability of ViT-DINO with the spatial precision of cycle consistency. GLU-Net [65] incorporates cycle consistency as a post-processing step to filter the output of the global correlation, ensuring reciprocal matching.

Instead of relying on the consistency between two images, some methods create a longer consistency path by image augmentation. WarpC [69] introduces warp consistency, a weakly-supervised objective for dense flow regression. It enforces flow constraints using a third image, generated by randomly warping one of the original pairs, forming an image triplet to capture flow consistency. Furthermore, PWarpC [106] extends the warp-supervision constraint introduced in WarpC into a probabilistic form, enhancing robustness and performance. Zhou *et al.* [107] incorporated a 3D CAD model to enforce cycle consistency between synthetic and real images. This method forms a 4-cycle flow field, where correspondences between real images and rendered ones act as a supervisory signal for training. CycleGAN [108], similar to Zhou *et al.* [107], combines cycle consistency loss with adversarial loss to learn transformations between source and target domains without requiring paired samples.

Consistency-based methods offer implicit supervision on local correspondence matching, improving accuracy and smoothness of dense matching between two images when compared with plain image-level supervision introduced in the previous section. However, without keypoint labels, they still underperform supervised methods in terms of correspondence precision. This inspires the pseudo-label generation-based methods that enhance the training signal based on sparse keypoint labels.

3) *Pseudo-Label Generation*: The majority of methods in Section III-C are supervised paradigms trained directly on sparse keypoint annotations provided by the dataset. While these methods excel in metrics that measure the precision of sparse keypoint localization, they may suffer from generalization issues due to overfitting to the specific keypoint positions of the training data. To address this limitation, pseudo-label generation methods expand supervision beyond these specific locations by incorporating pseudo labels. These pseudo labels can take various forms, such as cost volumes or flow maps, serving as complementary signals to sparse ground-truth labels. By diversifying the supervision region, they enhance model accuracy and robustness.

PMD [109] proposes a probabilistic teacher-student framework to perform knowledge distillation. It generates pseudo semantic flows on unlabeled real image pairs using a teacher model trained on synthetic data, and then trains a student model with its predictions. It demonstrates that the knowledge for semantic correspondence learned from synthetic data can be transferred to real data through this distillation process. Unlike PMD [109], SCorrSAN [75] directly learns dense flows from real image pairs labeled with sparse keypoints. It generates dense pseudo-labels for unlabeled region by

TABLE I  
BENCHMARK DATASETS FOR SEMANTIC CORRESPONDENCE. “SOURCE DATASETS” REPRESENT ORIGINAL DATASETS WHERE IMAGES OF THE DATASET ARE SAMPLED FROM.

Dataset Name	Year	Pairs	Class	Source datasets	Annotations	Characteristics
Caltech-101 [38]	2006	1,515	101	Caltech-101 [112, 113]	object segmentation	tightly cropped images of objects, little background
PASCAL-PARTS [102]	2015	4700	20	PASCAL-PARTS [114]	keypoints (0~12), azimuth, elevation, cyclo-rotation, body part segmentation	tightly cropped images of objects, little background, part and 3D information
TSS [115]	2016	400	9	FG3DCar, JODS, PASCAL [116–118]	flows and foreground masks for image pair	dense flow field annotations obtained by interpolating sparse keypoint matches with additional co-segmentation masks
PF-WILLOW [42]	2017	900	5	PASCAL VOC 2007, Caltech-256 [119–121]	keypoints (10)	center-aligned images, pairs with the same viewpoint
PF-PASCAL [42]	2017	1,300	20	PASCAL VOC 2007 [119]	keypoints (4~17), bbox.	pairs with the same viewpoint
SPair-71k [13, 122]	2019	72,758	18	PASCAL3D+, PASCAL VOC 2012 [119, 123]	keypoints (3~30), azimuth, view-point diff., scale diff., trunc. diff., occl. diff., object seg., bbox.	large-scale data with diverse variations, rich annotations, clear dataset splits
AP-10K [124]	2021	29k	47	public datasets focusing on animals [125–132]	keypoints (3~17), bbox.	challenging wild environments and substantial data across multiple supervision settings
MISC210K [133]	2022	218,179	34	MS COCO	keypoint (5~52), bounding box, instance mask, text description	multiple object, more challenging variations, such as mutual occlusion of multiple objects and perspective distortions in complex scenes
SC-ImageNet [100]	2023	794,612	679	ImageNet	32 pseudo keypoint pairs for each image pair	can be used for model pre-training, provide pixel-level matching relationships in image pairs

expanding the sparse annotations to surrounding regions using spatial-smoothness assumptions, then iteratively selects the most reliable predictions following the small-loss principle [110]. MatchMe [111] argues that previous approaches attempting to densify keypoints for training may not effectively address the data-hungry nature of these tasks. To overcome this limitation, MatchMe [111] proposes to leverage the rich semantic information available in large corpora of unlabeled image pairs. It first trains a teacher model using the labeled data, this teacher then generates pseudo-correspondences for unlabeled image pairs. The student model is subsequently trained using pseudo-labels as supervision. To progressively enhance label quality, it iteratively updates the teacher with the refined student model through multiple training cycles.

Unlike the aforementioned approach [75, 100, 109, 111] that uses flow maps as pseudo-labels, SemiMatch [74] and SC-ImageNet [100] utilize the cost volume both as ground-truth correspondences and as the format for pseudo-labels. In SemiMatch [74] framework, given source image  $I^s$  and target image  $I^t$ , the target image is first augmented into a weakly-augmented version and a strongly-augmented version through photometric and geometric augmentations, forming a triplet of images. The model then predicts the cost volume between the source image and the weakly-augmented target image supervised by keypoint annotations. This cost volume is then transformed by applying the same geometric warp used for the strong augmentation, and sharpened to generate a pseudo-label. The pseudo-label is subsequently used to supervise the generation of the cost volume in the strong-augmented branch. Huang *et al.* [100] proposed learning correspondences

from image-level annotations and created a new dataset called Semantic Correspondence ImageNet (SC-ImageNet), which contains high-quality pseudo-labels for semantic correspondence.

These pseudo-label generation-based methods demonstrate unique advantages in semantic correspondence tasks by combining sparse keypoint annotations with generated pseudo-labels. Through the complementary signals provided by pseudo-labels, some of these approaches outperform purely supervised methods in certain scenarios. However, these methods have not completely eliminated the dependency on manual annotations—model training still requires high-quality sparse keypoint annotations as initial conditions. Moreover, the quality of pseudo-labels heavily relies on the accuracy of the initial supervisory signals, which may lead to error propagation issues. Despite these limitations, pseudo-label generation-based methods represent a research direction that has achieved an effective balance between reducing annotation dependency and enhancing model performance.

#### IV. DATASETS AND EVALUATION METRICS

This section reviews benchmark datasets and evaluation metrics for semantic correspondence. We first present prevalent datasets spanning from early small-scale collections to modern large-scale benchmarks, detailing their annotation formats and applications. Subsequently, we formalize the standard Percentage of Correct Keypoints (PCK) metric with its dataset-specific variants, clarifying its computation methods and practical implementations across different datasets.

### A. Datasets for Semantic Correspondence

Many datasets have been released for benchmarking the semantic matching model. We summarize the year of release, number of image pairs, number of object classes, image sources, and types of annotations in Table I. We also briefly introduce some of them as below.

**Caltech-101** [38] dataset provides binary mask annotations of objects of interest for 1,515 image pairs, enabling evaluations of coarse-level semantic correspondence tasks. This dataset contains images from 101 distinct object categories, each paired with a ground-truth foreground segmentation mask. Although initially designed for image classification, this dataset has been repurposed for evaluating semantic alignment.

**TSS** [115] dataset uniquely provides dense flow field annotations for the foreground objects in its image pairs. It contains 400 image pairs of 7 object categories, divided into three groups based on their source datasets: FG3DCAR [116], JODS [117], and PASCAL[118].

**PF-WILLOW** [42] dataset consists of 900 image pairs of five object classes: face, car, motorbike, duck, and wineBottle. Each image is annotated with 10 keypoints, making this dataset well-suited for evaluating semantic correspondence methods, particularly those focused on keypoint-level matching between similar object instances.

**PF-PASCAL** [42] dataset consists of 1,300 image pairs drawn from the PASCAL VOC dataset [119], covering 20 object classes. Each image is annotated with between 4 and 17 keypoints, as well as bounding boxes.

**SPair-71k** [13, 122] is a large-scale and comprehensive benchmark dataset for semantic correspondence, consisting of 70,958 image pairs across 18 object categories and encompassing a broad range of viewpoint and scale variations. Compared to earlier datasets, SPair-71k [122] notably increases the number of image pairs and provides more accurate and detailed annotations. The annotations capture variations in viewpoint, scale, truncation, and occlusion.

**AP-10K** [124] was originally designed for animal pose estimation, consisting of 10,015 images spanning 23 families and 54 species. Zhang *et al.*[29] adapted this dataset into a challenging semantic correspondence benchmark, resulting in 260,950 training pairs, 20,630 testing pairs, and 8,816 validation pairs. The validation and testing subsets are organized into three distinct settings: an intra-species set, a cross-species set, and a cross-family set. Overall, this dataset is approximately five times larger than SPair-71k [13, 122], offering a broader and more complex evaluation environment.

### B. Evaluation Metrics

The Percentage of Correct Keypoints (PCK) metric serves as a standard measure for evaluating the performance of keypoint matching in semantic correspondence tasks. Given an image pair  $(I^s, I^t)$  and its associated correspondence set  $\mathcal{X} = \{(\mathbf{x}_q^s, \mathbf{x}_q^t) \mid q = 1, 2, \dots, n\}$ , where  $\mathbf{x} = (x, y)$ ,  $\mathbf{x}_q^s$  is the query point on the source image  $I^s$  and  $\mathbf{x}_q^t$  is the ground-truth correspondence on the target image  $I^t$ , we find its predicted

correspondence  $\{\bar{\mathbf{x}}_q^t \mid q = 1, 2, \dots, n\}$  and calculate PCK for the image pair by:

$$PCK(I^s, I^t) = \frac{1}{n} \sum_{q=1}^n \mathbb{I}(\|\bar{\mathbf{x}}_q^t - \mathbf{x}_q^t\| \leq \alpha * \theta),$$

where  $\theta$  is a base threshold,  $\alpha$  is a value less than 1, and  $\mathbb{I}(\cdot)$  is the binary indicator function with  $\mathbb{I}(\text{true}) = 1$  and  $\mathbb{I}(\text{false}) = 0$ . The widely used values for  $\alpha$  include 0.05, 0.1 or 0.15 and the base threshold  $\theta$  is usually associated with each dataset:

- **SPair-71k** and **AP-10K**: The base threshold is defined by the object’s bounding box dimensions:  $\theta_{\text{bbox}} = \max(h_{\text{bbox}}, w_{\text{bbox}})$ , where  $h_{\text{bbox}}$  and  $w_{\text{bbox}}$  denote the height and width of the bounding box.
- **PF-PASCAL**: The base threshold is determined by the image dimensions:  $\theta_{\text{img}} = \max(h_{\text{img}}, w_{\text{img}})$ .
- **PF-WILLOW**: The base threshold uses the keypoint-based bounding box (bbox-kp) PCK:  $\theta_{\text{kps}} = \max(\max_q(x_q^t) - \min_q(x_q^t), \max_q(y_q^t) - \min_q(y_q^t))$ , where the bounding box is approximated from the keypoint positions, resulting in a tighter fit around the object.

There are two ways to report PCK value. One common practice is to calculate a PCK value for each image and then average it across the dataset or across each category split. The other approach calculates PCK by dividing the total number of correctly predicted points over the entire dataset (or each category split) by the total number of predicted points. We refer to the former as “PCK per image” and the latter as “PCK per point”. In this paper, we align with the majority of previous studies by adopting “PCK per image” as our evaluation metric.

## V. BENCHMARK OF EXISTING METHODS

We compare the performance of existing methods on the SPair-71k, PF-PASCAL, and PF-WILLOW datasets and categorize them into three groups: supervised methods, weakly supervised methods, and zero-shot methods. Methods that utilize keypoint annotations are classified as supervised methods, and their performance is summarized in Table II. Methods that do not use keypoint annotations but use other auxiliary annotations, such as class labels, image pairs, or masks, are categorized as weakly supervised methods, and their performance is presented in Table III. Finally, methods without any fine-tuning are referred to as zero-shot methods, and their performance is shown in Table IV.

The quantitative comparison result reveals that supervised methods significantly outperform weakly supervised and zero-shot approaches, as they leverage keypoint annotations for fine-tuning. Within supervised methods, vision transformer foundation models (e.g., DINO) and stable diffusion backbones demonstrate superior performance compared to CNN backbones like ResNet. This advantage stems from transformers’ global interaction capabilities and their exposure to larger-scale pre-training datasets, which provide stronger initialization. Due to the diversity of the backbone, matching modules, and inconsistent image resolution, it is hard to conclude the most effective choice for each component in semantic

TABLE II  
PERFORMANCE COMPARISON OF SUPERVISED METHODS ON SPAIR-71K, PF-PASCAL, AND PF-WILLOW DATASETS. THE METHODS ARE CATEGORIZED INTO TWO GROUPS BASED ON THE BACKBONE USED: CNN (E.G., RESNET-101) AND FOUNDATION MODEL (E.G., DINO, SD). FT.: FINE-TUNE, ML.: MULTI LAYER FEATURE, AUG.: DATA AUGMENTATION, RESO.: RESOLUTION.

Methods	Backbone	FT.	ML.	Aug.	Reso.	SPair-71k			PF-PASCAL			PF-WILLOW					
						PCK @ $\alpha_{\text{bbox}}$			PCK @ $\alpha_{\text{img}}$			PCK @ $\alpha_{\text{bbox}}$			PCK @ $\alpha_{\text{bbox-kp}}$		
						0.05	0.1	0.15	0.05	0.1	0.15	0.05	0.1	0.15	0.05	0.1	0.15
SCNet [11]	VGG16	×	×	×	224	-	-	-	36.2	72.2	82.0	38.6	70.4	85.3	-	-	-
NC-Net [17]	ResNet-101	✓	×	×	-	-	20.1	-	54.3	78.9	86.0	-	-	-	33.8	67.0	-
CNNGeo [94]	ResNet-101	×	×	×	227	-	20.6	-	41.0	69.5	80.4	-	-	-	36.9	69.2	-
WeakAlign [79]	ResNet-101	×	×	×	-	-	20.9	-	49.0	74.8	84.0	-	-	-	37.0	70.2	-
A2Net [95]	ResNet-101	×	×	×	-	-	22.3	-	42.8	70.8	83.3	-	-	-	36.3	68.8	-
HPF [13]	ResNet-101	×	✓	×	-	-	28.2	-	60.1	84.8	92.7	45.9	74.4	85.6	45.9	74.4	85.6
ANC-Net [18]	ResNeXt-101	×	×	×	-	-	30.1	-	-	88.7	-	-	-	-	-	-	-
DHPF [14]	ResNet-101	×	✓	×	240	20.9	37.3	47.5	75.7	90.7	95.0	49.5	77.6	89.1	-	71.0	-
PMD [109]	ResNet-101	✓	-	-	-	-	37.4	-	-	90.7	-	-	75.6	-	-	-	-
CHM [19]	ResNet-101	✓	×	×	240	27.2	46.3	57.5	80.1	91.6	94.9	52.7	79.4	87.5	-	69.6	-
CATs [21]	ResNet-101	✓	✓	✓	256	27.7	49.9	61.7	75.4	92.6	96.4	50.3	79.2	90.3	40.7	69.0	-
PMNC [20]	ResNet-101	✓	✓	×	400	-	50.4	-	82.4	90.6	-	-	-	-	-	-	-
MMNet-FCN [54]	ResNet-101	✓	✓	×	224	33.3	50.4	61.2	81.1	91.6	95.9	-	-	-	-	-	-
SemiMatch [74]	ResNet-101	✓	-	✓	256	-	50.7	-	80.1	93.5	96.6	54.0	82.1	92.1	-	-	-
CHMNet [78]	ResNet-101	✓	✓	✓	240	-	51.3	-	83.1	92.9	-	53.8	79.3	-	-	69.3	-
PWarpC-NC-Net [106]	ResNet-101	-	-	-	Ori	31.6	52.0	-	67.8	82.3	86.9	-	-	-	46.1	72.6	82.7
NeMF [93]	ResNet-101	-	-	-	Ori	34.2	53.6	-	80.6	93.6	-	-	-	-	60.8	75.0	-
TransforMatcher [23]	ResNet-101	✓	✓	✓	240	32.4	53.7	-	80.8	91.8	-	-	76.0	-	-	65.3	-
HCCNet [16]	ResNet-101	✓	✓	✓	240	35.8	54.8	-	80.2	92.4	-	-	74.5	-	-	65.5	-
SCorrSAN [75]	ResNet-101	✓	×	✓	256	-	55.3	-	81.5	93.3	96.6	54.1	80.0	89.8	-	-	-
VAT [91]	ResNet-101	✓	✓	✓	-	35.0	55.5	65.1	78.2	92.3	96.2	52.8	81.6	91.4	42.3	71.3	-
KBCNet [55]	ResNet-101	✓	-	-	256	39.1	59.1	68.2	78.1	93.8	97.2	56.4	84.7	93.5	-	-	-
CATs++ [22]	ResNet-101	✓	✓	✓	512	40.7	59.8	68.5	84.9	93.8	96.8	56.7	81.2	-	47.0	72.6	-
MatchMe-CATs++ [111]	ResNet-101	✓	✓	✓	-	-	62.0	-	84.9	94.3	96.7	59.6	83.6	92.9	-	-	-
UFC [134]	ResNet-101	×	✓	✓	Ori	48.5	64.4	72.1	88.0	94.8	97.9	58.6	81.2	-	50.4	74.2	-
DINO-ViT [135]	DINO-ViT	-	✓	✓	-	-	61.4	-	-	-	-	-	-	-	-	-	-
ACTR [72]	iBOT	-	×	-	-	42.0	62.1	-	81.2	94.0	97.0	-	87.2	-	-	79.9	-
SimSC-iBOT [58]	iBOT	✓	×	×	256	43.0	63.5	-	88.4	95.6	97.3	-	-	-	44.9	71.4	84.5
DHF [57]	SD+DINOv2	✓	✓	-	Ori	-	64.6	-	-	86.7	-	-	78.0	-	-	-	-
LPMFlow [56]	ViT-B/16	✓	✓	-	256	46.7	65.6	-	82.4	94.3	97.2	-	87.6	-	-	81.0	-
SD4Match [28]	SD+DINOv2	×	×	×	768	59.5	75.5	-	84.4	95.2	97.5	-	-	-	52.1	80.4	91.2
GeoAware-SC [29]	SD+DINOv2	-	✓	×	960,840	72.6	82.9	-	85.5	95.1	97.4	-	-	-	-	-	-

TABLE III  
PERFORMANCE COMPARISON OF WEAKLY SUPERVISED METHODS ON SPAIR-71K, PF-PASCAL, AND PF-WILLOW DATASETS. FT.: FINE-TUNE, ML.: MULTI LAYER FEATURE, AUG.: DATA AUGMENTATION, RESO.: RESOLUTION.

Methods	Backbone	FT.	ML.	Aug.	Reso.	SPair-71k			PF-PASCAL			PF-WILLOW					
						PCK @ $\alpha_{\text{bbox}}$			PCK @ $\alpha_{\text{img}}$			PCK @ $\alpha_{\text{bbox}}$			PCK @ $\alpha_{\text{bbox-kp}}$		
						0.05	0.1	0.15	0.05	0.1	0.15	0.05	0.1	0.15	0.05	0.1	0.15
Semantic-GLU-Net [65]	VGG-16	-	✓	-	-	-	14.3	-	46.0	70.6	-	-	-	-	-	-	-
SAM-Net [76]	VGG-19	✓	-	-	-	-	-	-	60.1	80.2	86.9	-	-	-	-	-	-
WarpC [69]	VGG-16	×	✓	✓	-	-	23.5	-	62.1	81.7	89.7	49.0	75.1	86.9	-	-	-
PARN [97]	ResNet-101	✓	✓	✓	-	-	-	-	26.8	49.1	66.2	-	-	-	-	-	-
WeakMatchNet [104]	ResNet-101	✓	×	✓	-	-	-	-	-	78.0	-	49.1	81.9	92.2	-	-	-
DCCNet [15]	ResNet-101	×	×	×	400	-	-	-	55.6	82.3	90.5	43.6	73.8	86.5	-	-	-
CNNGeo [94]	ResNet-101	-	×	-	-	-	18.1	-	-	71.9	-	36.9	69.2	77.8	-	-	-
A2Net [95]	ResNet-101	-	×	-	-	-	20.1	-	42.8	70.8	83.3	36.3	68.8	84.4	-	-	-
WeakAlign [79]	ResNet-101	✓	×	✓	-	-	21.1	-	-	75.8	-	37.0	70.2	79.9	-	-	-
RTNs [96]	ResNet	×	×	×	-	-	25.7	-	55.2	75.9	85.2	-	-	-	41.3	71.9	86.2
SFNet [1, 2]	ResNet-101	×	✓	×	-	-	26.3	-	53.6	81.9	90.6	-	73.5	-	46.3	74.0	-
NC-Net [17]	ResNet-101	✓	×	×	400	-	26.4	-	54.3	78.9	86.0	44.0	72.7	85.4	-	-	-
PMD [109]	ResNet-101	✓	-	-	320	-	26.5	-	-	81.2	-	-	74.7	-	-	-	-
DHPF [14]	ResNet-101	×	✓	×	240	-	27.7	-	56.1	82.1	91.1	50.2	80.2	91.1	-	-	-
ASYM [136]	ResNet-50	×	-	-	-	-	34.0	-	-	-	-	-	-	-	-	-	-
GSF [73]	ResNet-101	×	✓	×	-	-	36.1	-	65.6	87.8	95.9	47.0	75.8	88.9	49.1	78.7	-
PWarpC-NC-Net [106]	ResNet-101	✓	✓	✓	Ori	18.5	38.0	-	61.7	82.6	88.5	-	-	-	43.6	74.6	86.9
ASIC [137]	ViT-S/8	×	-	-	-	-	36.9	-	-	-	-	53.0	76.3	-	-	-	-
SC-ImageNet [100]	iBOT-B	×	-	-	-	-	60.3	-	80.5	93.0	96.7	57.1	85.1	94.1	-	-	-

TABLE IV  
PERFORMANCE COMPARISON OF ZERO-SHOT METHODS ON SPAIR-71k, PF-PASCAL, AND PF-WILLOW DATASETS.

Methods	Backbone	Reso.	SPair-71k			PF-PASCAL			PF-WILLOW					
			PCK @ $\alpha_{\text{bbox}}$			PCK @ $\alpha_{\text{img}}$			PCK @ $\alpha_{\text{bbox}}$			PCK @ $\alpha_{\text{bbox-kp}}$		
			0.05	0.1	0.15	0.05	0.1	0.15	0.05	0.1	0.15	0.05	0.1	0.15
SCOT [138]	ResNet-101	Max 300	-	35.6	-	63.1	85.4	92.7	47.8	76.0	87.1	47.8	76.0	-
DINO+LiFT [60]	DINO(ViT-S/16)	-	14.7	28.7	-	-	-	-	-	-	-	-	-	-
LDM [59]	SD	-	28.9	45.4	-	-	-	-	53.0	84.3	-	-	-	-
DIFTsd [26]	SD	768	-	52.9	-	-	-	-	-	-	-	-	-	-
SD-DINO [27]	SD+DINOv2	960, 840	-	59.3	-	73.0	86.1	91.1	-	-	-	-	-	-
GeoAware-SC [29]	SD+DINOv2	960, 840	45.3	61.3	-	74.0	86.2	90.7	-	-	-	-	-	-

960, 840 represent image resolutions:  $960 \times 960$  for SD and  $840 \times 840$  for DINOv2, respectively.

matching. Therefore, we conduct extensive experiments in the next section to make fair and controlled evaluations of each stage in the matching pipeline and find out the most effective design of the model.

## VI. EXPERIMENTS AND ANALYSIS

This section evaluates each stage of semantic correspondence methods through detailed experiments. We begin by evaluating commonly used feature backbones in Section VI-A. We then pick the most effective one to serve as the foundation and evaluate popular matching modules, including both feature enhancement (Section VI-B) and matching refinement (Section VI-C) techniques, by appending them to it under standardized settings. Based on the experiment results, we present a strong and effective baseline in Section VI-E that achieves state-of-the-art performance in various benchmarks.

### A. Feature Backbone Evaluation

Due to the absence of systematic evaluation on the performance of commonly used feature backbones, in this section, we evaluate the performance of various feature backbones in a uniform setting to find out the most effective one. We select ResNet-101 [139], CLIP [140], iBOT [141], DINO [135], DINOv2 [24], and Stable Diffusion [25] as our choices for the backbone. Specifically, for ResNet-101, we truncate it before layer 4 following the literature convention [17, 18, 58]. For transformer backbones CLIP, DINO, iBOT, and DINOv2, we select CLIP-ViT-L/14, DINO-ViT-B/16, iBOT-ViT-B/16, DINOv2-ViT-B/14 configurations respectively. For stable diffusion based backbone, we follow the setup in DIFT [28] and use Stable Diffusion 2-1 as the model. Moreover, we also evaluate the combined backbone SD+DINO [27] by concatenating the feature maps from SD2-1 and DINOv2 along the channel dimension. Due to the inconsistent image-to-feature ratio across different backbones, we evaluate all backbones on three commonly adopted feature maps resolutions:  $16 \times 16$ ,  $32 \times 32$ , and  $60 \times 60$ .

1) *Zero-Shot Evaluation*: We conduct zero-shot evaluations to assess the performance of different feature backbones across varying feature map sizes. The results are presented in Table V. As shown, SD2-1, DINOv2, and their combined variant (SD2-1+DINOv2) significantly outperform CLIP, ResNet-101, DINOv1, and iBOT. We attribute this superiority to their pre-training on larger-scale datasets, which enhances feature generalization. Notably, the combination of SD2-1 and DINOv2

TABLE V  
EVALUATION OF ZERO-SHOT FEATURE BACKBONES ON THE SPAIR-71k DATASET. RESO.: IMAGE RESOLUTION, FEATURE MAP SIZE.

Backbone	Reso.	SPair-71k			
		PCK @ $\alpha_{\text{bbox}}$			
		0.01	0.05	0.1	0.15
CLIP	224, 16	0.5	9.5	22.8	33.2
ResNet-101	960, 60	3.3	18.6	26.5	32.2
ResNet-101	512, 32	1.6	16.5	26.8	33.1
ResNet-101	256, 16	0.5	10.3	23.0	31.7
DINOv1	960, 60	1.7	14.0	25.6	35.3
DINOv1	512, 32	1.4	15.8	30.2	40.2
DINOv1	256, 16	0.6	12.2	27.8	38.8
iBOT	960, 60	2.2	18.7	33.8	44.9
iBOT	512, 32	1.8	21.4	38.9	50.3
iBOT	256, 16	0.9	16.2	35.1	47.7
SD2-1	960, 60	7.5	40.0	50.7	56.7
SD2-1	512, 32	3.2	29.4	41.8	48.0
SD2-1	256, 16	0.5	9.7	21.0	28.7
DINOv2	840, 60	7.3	40.0	54.4	62.8
DINOv2	448, 32	3.7	35.4	52.9	62.2
DINOv2	224, 16	1.1	20.9	43.1	56.2
SD2-1+DINOv2	(960,840), 60	9.7	47.9	<b>60.4</b>	67.0
SD2-1+DINOv2	(512,448), 32	4.7	40.3	<u>56.5</u>	64.1
SD2-1+DINOv2	(256,224), 16	1.3	21.4	41.9	53.1

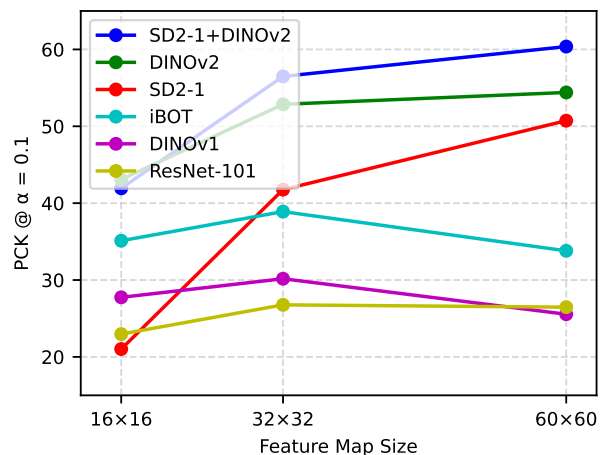


Fig. 7. Performance of different feature backbones on zero-shot evaluation across varying feature map sizes ( $16 \times 16$ ,  $32 \times 32$ , and  $60 \times 60$ ).

TABLE VI  
EVALUATION OF FINE-TUNING FEATURE BACKBONES ON THE SPAIR-71K DATASET. RESO.: IMAGE RESOLUTION, FEATURE MAP SIZE.

Backbone	Reso.	SPair-71k			
		PCK @ $\alpha_{\text{bbox}}$			
		0.01	0.05	0.1	0.15
SD-CPM	960, 60	11.2	62.0	75.4	80.6
SD-CPM	512, 32	4.4	46.6	69.3	77.9
SD-CPM	256, 16	0.4	7.5	22.1	35.4
SD-CPM+DINOv2	(960,840), 60	12.4	62.0	76.0	81.2
SD-CPM+DINOv2	(512,448), 32	5.5	49.4	70.4	78.7
SD-CPM+DINOv2	(256,224), 16	1.6	25.9	51.7	65.2
DINOv2	840, 60	15.0	67.4	<b>81.7</b>	87.1
DINOv2	448, 32	7.1	56.2	<u>76.6</u>	84.3
DINOv2	224, 16	1.9	30.5	58.2	72.1

TABLE VII  
EVALUATION OF FINE-TUNING DIFFERENT STAGES OF DINOv2 ON THE SPAIR-71K DATASET. FF.: FINE-TUNE FROM, RESO.: IMAGE RESOLUTION, FEATURE MAP SIZE.

Backbone	FF.	Reso.	SPair-71k			
			PCK @ $\alpha_{\text{bbox}}$			
			0.01	0.05	0.1	0.15
DINOv2	-	840, 60	7.3	40.0	54.4	62.8
DINOv2	stage12	840, 60	15.0	67.4	81.7	87.1
DINOv2	stage11	840, 60	17.5	73.3	<b>85.1</b>	89.3
DINOv2	stage10	840, 60	16.6	73.2	<u>84.5</u>	88.2
DINOv2	stage9	840, 60	17.8	73.1	84.0	87.8
DINOv2	stage8	840, 60	16.7	70.9	82.2	86.3

achieves the highest performance, aligning with the findings of SD-DINO [27], which emphasize the complementary strengths of these two models. To further analyze resolution impacts, we plot performance against feature map sizes in Figure 7. We find that ResNet101, DINOv1, and iBOT exhibit minimal or negative gains when the resolution increases to  $60 \times 60$  from  $32 \times 32$ . In contrast, SD2-1 and DINOv2 show consistent improvements with higher resolutions. We hypothesize this stems from two factors: (1) ResNet’s local receptive fields limit global context capture, and (2) fixed positional encodings in DINOv1 and iBOT hinder adaptation when interpolated to larger spatial dimensions.

2) *Strongly Supervised Evaluation*: To systematically analyze the adaptability of these backbones to semantic correspondence tasks, we also explore how the fine-tuning improves backbone performance. We select top-performing backbones in the zero-shot evaluation, SD2-1, DINOv2, and SD2-1+DINOv2, for this experiment because the rest options are less likely to achieve a higher performance due to their low zero-shot accuracies. Specifically, for SD2-1, we adopt the SD4Match [28] framework by fine-tuning its conditional prompting module (SD-CPM). For DINOv2, we fine-tune the last stage of the model. For the combination of SD2-1 and DINOv2, we concatenate the feature maps from them along the channel dimension, and jointly optimize the conditional prompting module of SD2-1 and the final stage of DINOv2. We follow the learning framework in SimSC [58], using the cross-entropy loss between the query point and the entire target

feature map as the training loss.

The strongly supervised evaluation results are presented in Table VI. Fine-tuning the final stage of DINOv2 at an input resolution of  $840 \times 840$  yields superior performance across all thresholds, achieving a PCK of 81.74 at  $\alpha_{\text{bbox}} = 0.1$ . Notably, while the combination of SD2-1 and DINOv2 showed complementary advantages in the zero-shot setting, DINOv2 alone outperforms this combination under fine-tuning. We speculate that during the fine-tuning process, the complementary nature of these features might be diminished, with SD2-1 features possibly becoming the dominant influence, thus limiting the overall performance.

As DINOv2 demonstrates its superiority, we further explore fine-tuning more stages of DINOv2. The results are summarized in Table VII. Notably, we observe that the performance peaks when fine-tuning up to stage 11, achieving the highest PCK scores, but declines when deeper layers are fine-tuned. This phenomenon could be attributed to the increased number of trainable parameters in deeper layers. While these parameters help the model better fit the matching task, they also increase the risk of overfitting to training data, thereby compromising the model’s generalization ability and resulting in decreased performance on unseen data.

**Takeaways: DINOv2 is the most powerful feature backbone for semantic correspondence.** According to Table VI, DINOv2 demonstrates best performance across different resolutions, demonstrating its versatility in adapting to varying input sizes while maintaining high performance. Its self-supervised pre-training strategy enables the learning of highly generalizable feature representations, making it particularly beneficial for semantic correspondence. **Fine-tuning feature backbones plays a crucial role in performance enhancement.** As demonstrated in Table VII, task-specific adaptation of DINOv2 significantly improves performance: fine-tuning its last two transformer blocks at  $840 \times 840$  resolution achieves a PCK@0.1 score of 85.11%, marking a 30% improvement over the zero-shot performance. **For DINOv2, larger image sizes improve semantic correspondence performance.** Results from Table V and Table VI suggest that higher image resolutions may enhance performance by preserving finer spatial details, which could enable more precise semantic correspondence.

## B. Feature Enhancement Evaluation

After fine-tuning the feature backbone, we explore how feature enhancement techniques and matching refinement modules may further improve matching accuracy. We select DINOv2 as the feature backbone and investigate two commonly used feature enhancement architectures: CNN architecture [1, 2, 29, 75] and transformer architecture [90]. For the CNN approach, we adopt the standard ResNet Bottleneck Block architecture with 768 input/output channels and a bottleneck dimension of 192 channels (1/4 reduction ratio). Similarly, for the transformer approach, we adopt a transformer block with 768 feature dimensions and linear attention mechanism for efficient computation. The block consists of standard multi-head self-attention layers followed by a two-layer MLP with

TABLE VIII

EVALUATION OF DIFFERENT FEATURE ENHANCEMENT MODULES ON THE SPAIR-71K DATASET. THE METHODS ARE CATEGORIZED INTO TWO TYPES: FROZEN DINOv2 BACKBONE AND JOINT TRAINING OF THE LAST LAYER OF DINOv2 AND THE FEATURE ENHANCEMENT MODULE. THE HIGHEST PCK VALUES ARE HIGHLIGHTED IN BOLD, WHILE BASELINE METHODS (WITHOUT FEATURE ENHANCEMENT MODULE) ARE INDICATED IN GRAY. FT.: FINE-TUNE. RESO.: IMAGE RESOLUTION, FEATURE MAP SIZE.

Backbone	FT.	Bottleneck	Reso.	SPair-71k				$\Delta$ PCK@0.1
				PCK @ $\alpha_{\text{bbox}}$				
				0.01	0.05	0.1	0.15	
DINOv2	×	-	840, 60	7.3	40.0	54.4	62.8	-
DINOv2	×	ResNet Bottleneck Block	840, 60	10.3	60.2	75.2	81.3	+20.8
DINOv2	×	Self-Attention	840, 60	11.8	60.8	<b>76.5</b>	83.1	+22.1
DINOv2	×	Self+Cross Attention	840, 60	11.5	60.6	<u>76.3</u>	83.2	+21.9
DINOv2	✓	-	840, 60	15.0	67.4	<u>81.7</u>	87.1	-
DINOv2	✓	ResNet Bottleneck Block	840, 60	15.1	71.1	<b>84.2</b>	88.9	+2.4
DINOv2	✓	Self-Attention	840, 60	13.9	66.4	80.9	87.1	-0.8
DINOv2	✓	Self+Cross Attention	840, 60	14.5	66.3	80.9	87.0	-0.8

1536 hidden dimensions. The block operates in two modes: self-attention (intra-image feature interaction) and self+cross-attention (intra-image self-focus followed by cross-image interaction).

We evaluate these enhancements under two training strategies: frozen backbone and end-to-end joint training. In the latter case, only the final stage of DINOv2 is fine-tuned. The results are summarized in Table VIII, with additional experiments across different input resolutions presented in Appendix Table A1.

**Frozen Backbone:** With the DINOv2 backbone frozen, training the feature enhancement layers yields substantial performance gains, with PCK@0.1 improving by more than 20%. The performance variations across different enhancement techniques are marginal, suggesting that feature enhancement layers consistently boost representation quality regardless of their specific architecture when working with a frozen backbone.

**Joint Training:** When jointly fine-tuning the backbone and enhancement module, the performance gains brought by the enhancement module are limited. The ResNet Bottleneck Block achieves a modest gain of 2.42% in PCK@0.1, while the Attention Block shows no advantages and slightly degrades performance. This phenomenon may be attributed to the backbone’s final layer already serving as an effective feature enhancer and having largely saturated the potential for extra improvement. Therefore, it leaves minimal room for additional enhancement modules to provide further gains.

**Takeaway: Feature enhancement performance efficacy depends on training paradigm:** Table VIII shows that with frozen backbones, feature enhancement modules boost PCK@0.1 by over 20%. During joint training, gains diminish sharply (ResNet: +2.4%; attention: performance degradation), revealing architectural limitations in such settings.

### C. Matching Refinement Evaluation

After evaluating the feature enhancement modules, we proceed to analyze matching refinement methods. Prior research has predominantly focused on refining cost volume, as described in Section III-C2. These methods can be largely

categorized into CNN [17–19, 70, 78] and Transformer [21–23, 68, 91, 93] approaches. Therefore, we select the Neighbourhood Consensus Aggregator [17] for CNN methods, and both the CATs Aggregator [21] and Match-to-Match Aggregator [23] for Transformer approaches, as they represent the majority of the cost volume-based methods.

**Neighbourhood Consensus Aggregator.** While following the neighbourhood consensus module from NC-Net [17], our implementation differs in two aspects: we employ  $3 \times 3 \times 3 \times 3$  filters instead of the original  $5 \times 5 \times 5 \times 5$  filters, and halve the number of feature channels in the intermediate convolutional layers from 16 to 8. These modifications reduce the computational complexity while maintaining the essential functionality of neighborhood consensus filtering for match refinement.

**CATs Aggregator.** We adopt the cost aggregator architecture from CATs [21] but implement a simplified version, reducing it from six layers to a single layer. Given the significant computational demands of Transformer operations at high resolutions, we restrict our experiments to 448 and 224 resolution for this module. Complete experimental results across all resolutions are presented in Appendix Table A2.

**Match-to-Match Aggregator.** Another Transformer approach is the match-to-match attention module [23], which treats each spatial match as an attention unit. We follow the original experimental configuration in TransforMatcher [23].

The evaluation results are summarized in Table IX, with additional experiments across different input resolutions presented in Appendix Table A2. Neighbourhood consensus module consistently outperforms other cost aggregators on the SPair-71k dataset, demonstrating its superior capability in refining the cost volume and enhancing semantic matching performance. Regarding the CATs cost aggregator, it exhibits notable limitations: First, it cannot be applied to high-resolution inputs ( $840 \times 840$ ) due to computational constraints. Second, at  $448 \times 448$  resolution, it performs substantially worse than both NeighConsensus and Match2Match, with PCK@0.1 dropping by -3.4% and -5.2% in frozen and fine-tuned settings respectively, making it the least effective among the three aggregators.

TABLE IX  
EVALUATION OF COST AGGREGATION MODULE ON THE SPair-71k DATASET. THE METHODS ARE CATEGORIZED INTO TWO TYPES: FROZEN DINOv2 BACKBONE AND JOINT TRAINING OF THE LAST LAYER OF DINOv2 AND THE COST AGGREGATOR. THE BASELINE METHODS (WITHOUT COST AGGREGATOR) ARE INDICATED IN GRAY. FT.: FINE-TUNE. RESO.: IMAGE RESOLUTION, FEATURE MAP SIZE.

Backbone	FT.	Cost Aggregator	Reso.	SPair-71k				$\Delta$ PCK@0.1
				PCK @ $\alpha_{\text{bbox}}$				
				0.01	0.05	0.1	0.15	
DINOv2	×	-	840, 60	7.3	40.0	<u>54.4</u>	62.8	-
DINOv2	×	Match2Match	840, 60	6.8	39.5	54.1	62.6	-0.3
DINOv2	×	NeighConsensus	840, 60	6.2	45.8	<b>61.9</b>	69.3	+7.5
DINOv2	×	-	448, 32	3.7	35.4	<u>52.9</u>	62.2	-
DINOv2	×	CATs	448, 32	2.6	30.8	49.5	59.7	-3.4
DINOv2	×	Match2Match	448, 32	3.6	34.8	52.2	61.7	-0.7
DINOv2	×	NeighConsensus	448, 32	2.8	33.4	<b>56.5</b>	67.7	+3.6
DINOv2	✓	-	840, 60	15.0	67.4	81.7	87.1	-
DINOv2	✓	Match2Match	840, 60	13.9	68.3	<u>83.3</u>	88.6	+1.6
DINOv2	✓	NeighConsensus	840, 60	12.7	70.2	<b>85.2</b>	89.6	+3.5
DINOv2	✓	-	448, 32	7.1	56.2	76.6	84.3	-
DINOv2	✓	CATs	448, 32	3.2	42.6	71.4	82.4	-5.2
DINOv2	✓	Match2Match	448, 32	6.3	55.4	<u>77.8</u>	85.9	+1.2
DINOv2	✓	NeighConsensus	448, 32	5.0	54.7	<b>79.4</b>	87.3	+2.8

**Takeaway: CNN cost aggregators are more effective than Transformer aggregators.** CNN aggregators, such as Neighbourhood Consensus, consistently outperform Transformer counterparts as shown in Table IX, particularly at lower resolutions (e.g.,  $224 \times 224$ ), as shown in Appendix Table A2. This suggests that the local receptive field and hierarchical feature processing of CNN architectures are more suitable for cost volume refinement compared to the global attention mechanism of transformers.

#### D. Experimental Results Discussion

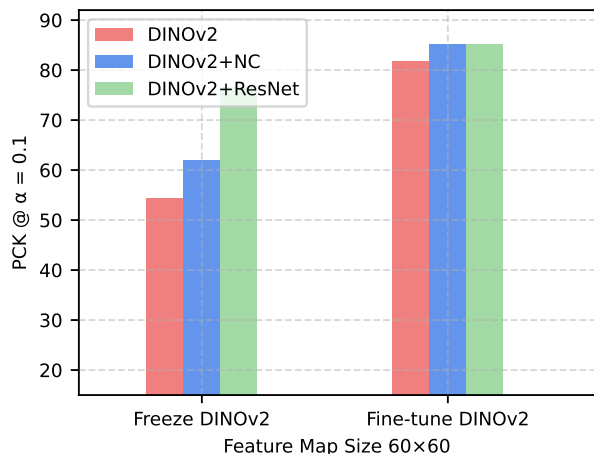


Fig. 8. Performance of ResNet bottleneck and neighbourhood consensus aggregator for frozen and fine-tuned DINOv2 with a feature map size of  $60 \times 60$ .

**Feature adaptation is more impactful than cost aggregation in the absence of backbone fine-tuning.** We compare effectiveness of ResNet feature enhancement module and neighbourhood consensus cost aggregator on DINOv2 backbone in Figure 8. Results show that with a frozen backbone, ResNet

feature enhancement brings larger performance gains than neighbourhood consensus cost aggregation.

**The backbone dominates the fundamental performance characteristics.** The experimental results presented in Section VI-B and Section VI-C demonstrate that joint training of DINOv2 with either bottlenecks or cost aggregators yields relatively modest performance improvements. These empirical findings indicate that the backbone’s feature extraction capability serves as a critical constraint on overall matching performance. This can be attributed to the backbone’s critical role in constructing the initial feature representations, which serve as a crucial foundation for subsequent matching quality.

#### E. A Strong Baseline

Based on our extensive experiments and analysis, we have constructed an effective semantic matching framework in both zero-shot and supervised settings. For zero-shot evaluation, we compare the best performing zero-shot model, SD2-1+DINOv2, against the literature in Table X. As demonstrated, despite the simpler architecture, our SD2-1+DINOv2 achieves comparable results to GeoAware-SC [29], showing the redundancy in the more complex designs in the literature.

In the supervised setting, we compare the best-performing backbone (DINOv2), feature enhancement design (DINOv2+ResNet), and matching filtering design (DINOv2+NC) against other methods in Table XI. Notably, by fine-tuning the last two layers of DINOv2 alone, we achieve the second-best performance on SPair-71k. When incorporating the ResNet bottleneck and the Neighbourhood Consensus cost aggregator, our approach attains state-of-the-art results on both SPair-71k and PF-PASCAL datasets.

Beyond these standard benchmarks, we further validate our approach on the AP-10K dataset (Table XII). Despite a simple architecture and straightforward training strategy, our method achieves comparable state-of-the-art result as well.

TABLE X  
PERFORMANCE COMPARISON OF ZERO-SHOT METHODS ON SPAIR-71K, PF-PASCAL, AND PF-WILLOW DATASETS. THE HIGHEST PCK VALUES ARE EMPHASIZED IN BOLD, WHEREAS THE SECOND HIGHEST ARE UNDERLINED.

Methods	Backbone	Reso.	SPair-71k			PF-PASCAL			PF-WILLOW		
			PCK @ $\alpha_{\text{bbox}}$			PCK @ $\alpha_{\text{img}}$			PCK @ $\alpha_{\text{bbox-kp}}$		
			0.05	0.1	0.15	0.05	0.1	0.15	0.05	0.1	0.15
LDM [59]	SD	-	28.9	45.4	-	-	-	-	-	-	-
DIFTsd [26]	SD	768	-	52.9	-	-	-	-	-	-	-
SD-DINO [27]	SD+DINOv2	960, 840	-	59.3	-	<u>73.0</u>	86.1	<u>91.1</u>	-	-	-
GeoAware-SC [29]	SD+DINOv2	960, 840	<u>45.3</u>	<b>61.3</b>	-	<b>74.0</b>	<u>86.2</u>	90.7	-	-	-
<b>Ours</b>	SD+DINOv2	960, 840	<b>47.9</b>	<u>60.4</u>	<b>67.0</b>	72.9	<b>88.3</b>	<b>93.4</b>	46.6	72.8	85.8

960, 840 represent image resolutions: 960×960 for SD and 840×840 for DINOv2, respectively.

TABLE XI  
PERFORMANCE COMPARISON OF SUPERVISED METHODS ON SPAIR-71K, PF-PASCAL, AND PF-WILLOW DATASETS. THE HIGHEST PCK VALUES ARE EMPHASIZED IN BOLD, WHEREAS THE SECOND HIGHEST ARE UNDERLINED. RESO.: RESOLUTION. DINOv2 + RESNET REFERS TO THE DINOv2 BACKBONE WITH ADDITIONAL RESNET BOTTLENECK. DINOv2 + NC REFERS TO THE DINOv2 BACKBONE WITH NEIGHBOURHOOD CONSENSUS COST AGGREGATOR.

Methods	Backbone	Reso.	SPair-71k			PF-PASCAL			PF-WILLOW		
			PCK @ $\alpha_{\text{bbox}}$			PCK @ $\alpha_{\text{img}}$			PCK @ $\alpha_{\text{bbox-kp}}$		
			0.05	0.1	0.15	0.05	0.1	0.15	0.05	0.1	0.15
SimSC-iBOT [58]	iBOT	256	43.0	63.5	-	<b>88.4</b>	<u>95.6</u>	97.3	44.9	71.4	84.5
DHF [57]	SD+DINOv2	Ori	-	64.6	-	-	86.7	-	-	-	-
LPMFlow [56]	ViT-B/16	256	46.7	65.6	-	82.4	94.3	97.2	-	<b>81.0</b>	-
SD-DINO [27]	SD+DINOv2	960, 840	-	74.6	-	80.9	93.6	96.9	-	-	-
SD4Match [28]	SD+DINOv2	768	59.5	75.5	-	84.4	95.2	<u>97.5</u>	<b>52.1</b>	<u>80.4</u>	<b>91.2</b>
GeoAware-SC [29]	SD+DINOv2	960, 840	72.6	82.9	-	85.5	95.1	97.4	-	-	-
<b>Ours(DINOv2)</b>	DINOv2	840	<b>73.3</b>	<u>85.1</u>	89.3	<u>87.6</u>	<b>95.8</b>	<b>98.2</b>	<u>48.8</u>	73.7	85.8
<b>Ours(DINOv2+ResNet)</b>	DINOv2	840	<u>72.7</u>	<b>85.2</b>	<u>89.3</u>	80.3	90.8	94.9	46.6	74.1	<u>87.1</u>
<b>Ours(DINOv2+NC)</b>	DINOv2	840	70.2	<b>85.2</b>	<b>89.6</b>	80.6	91.5	95.0	39.8	62.3	74.9

TABLE XII  
PERFORMANCE COMPARISON OF SUPERVISED METHODS ON THE AP-10K DATASET. RESO.: IMAGE RESOLUTION

Methods	Reso.	AP-10K			
		PCK @ $\alpha_{\text{bbox}}$			
		0.01	0.05	0.1	0.15
GeoAware-SC [29]	960,840	23.1	73.0	<b>87.5</b>	-
<b>Ours(DINOv2)</b>	840	<b>24.5</b>	<b>74.3</b>	87.4	92.2
<b>Ours(DINOv2+ResNet)</b>	840	<u>24.0</u>	<u>73.1</u>	86.7	<u>92.3</u>
<b>Ours(DINOv2+NC)</b>	840	21.1	72.8	<u>87.4</u>	<b>92.6</b>

## VII. CONCLUSION AND DISCUSSION

In this paper, we first present a comprehensive review of semantic correspondence methods and introduce a structured taxonomy that systematically categorizes existing approaches according to their architectural designs and training strategies. Through extensive controlled experiments across all stages of the pipeline, we then identify critical insights at each stage of the semantic matching model. Finally, based on these findings, we propose a simple yet effective baseline that achieves state-of-the-art performance on multiple benchmark datasets, including SPAIR-71k, PF-PASCAL, and AP-10K, establishing a solid foundation for future research.

While our work demonstrate the effectiveness of DINOv2’s feature extraction capabilities through fine-tuning, the full potential of foundation models remains largely untapped. Future

research could explore more effective adaptation techniques to better leverage foundation model features. In terms of training strategies, one possible direction is to further investigate pseudo-label generation techniques, so as to alleviate the reliance on large-scale manual annotations. These directions may advance the semantic matching from both architectural and training perspectives.

## REFERENCES

- [1] J. Lee, D. Kim, J. Ponce, and B. Ham, “Sfnet: Learning object-aware semantic correspondence,” in *CVPR*, 2019.
- [2] J. Lee, D. Kim, W. Lee, J. Ponce, and B. Ham, “Learning semantic correspondence exploiting an object-level prior,” *TPAMI*, 2022.
- [3] C. Liu, J. Yuen, and A. Torralba, “Sift flow: Dense correspondence across scenes and its applications,” *TPAMI*, 2011.
- [4] J. Lee, E. Kim, Y. Lee, D. Kim, J. Chang, and J. Choo, “Reference-based sketch image colorization using augmented-self reference and dense semantic correspondence,” in *CVPR*, 2020.
- [5] M. Geyer, O. Bar-Tal, S. Bagon, and T. Dekel, “Tokenflow: Consistent diffusion features for consistent video editing,” *arXiv preprint arXiv:2307.10373*, 2023.
- [6] J. Lu, X. Li, and K. Han, “Regiondrag: Fast region-based image editing with diffusion models,” in *ECCV*, 2024.
- [7] D. Ofri-Amar, M. Geyer, Y. Kasten, and T. Dekel, “Neural congealing: Aligning images to a joint semantic atlas,” in *CVPR*, 2023.
- [8] C. Mou, X. Wang, J. Song, Y. Shan, and J. Zhang, “DragonDiffusion: Enabling drag-style manipulation on diffusion models,” *arXiv preprint arXiv:2307.02421*, 2023.
- [9] M. Cho, S. Kwak, C. Schmid, and J. Ponce, “Unsupervised object discovery and localization in the wild: Part-based matching with bottom-up region proposals,” in *CVPR*, 2015.
- [10] N. Dalal and B. Triggs, “Histograms of oriented gradients for human detection,” in *CVPR*, 2005.

- [11] K. Han, R. S. Rezende, B. Ham, K.-Y. K. Wong, M. Cho, C. Schmid, and J. Ponce, "Scnet: Learning semantic correspondence," in *ICCV*, 2017.
- [12] S. Kim, D. Min, B. Ham, S. Jeon, S. Lin, and K. Sohn, "Fess: Fully convolutional self-similarity for dense semantic correspondence," in *CVPR*, 2017.
- [13] J. Min, J. Lee, J. Ponce, and M. Cho, "Hyperpixel flow: Semantic correspondence with multi-layer neural features," in *ICCV*, 2019.
- [14] —, "Learning to compose hypercolumns for visual correspondence," in *ECCV*, 2020.
- [15] S. Huang, Q. Wang, S. Zhang, S. Yan, and X. He, "Dynamic context correspondence network for semantic alignment," in *ICCV*, 2019.
- [16] S. Kim, J. Min, and M. Cho, "Efficient semantic matching with hypercolumn correlation," in *WACV*, 2024.
- [17] I. Rocco, M. Cimpoi, R. Arandjelović, A. Torii, T. Pajdla, and J. Sivic, "Neighbourhood consensus networks," in *NeurIPS*, 2018.
- [18] S. Li, K. Han, T. W. Costain, H. Howard-Jenkins, and V. Prisacariu, "Correspondence networks with adaptive neighbourhood consensus," in *CVPR*, 2020.
- [19] J. Min and M. Cho, "Convolutional hough matching networks," *CVPR*, 2021.
- [20] J. Y. Lee, J. DeGol, V. Fragoso, and S. N. Sinha, "Patchmatch-based neighborhood consensus for semantic correspondence," in *CVPR*, 2021.
- [21] S. Cho, S. Hong, S. Jeon, Y. Lee, K. Sohn, and S. Kim, "Cats: Cost aggregation transformers for visual correspondence," in *NeurIPS*, 2021.
- [22] S. Cho, S. Hong, and S. Kim, "Cats++: Boosting cost aggregation with convolutions and transformers," *TPAMI*, 2023.
- [23] S. Kim, J. Min, and M. Cho, "Transformatcher: Match-to-match attention for semantic correspondence," in *CVPR*, 2022.
- [24] M. Oquab, T. Darcet, T. Moutakanni, H. Vo, M. Szafraniec, V. Khalidov, P. Fernandez, D. Haziza, F. Massa, A. El-Nouby *et al.*, "DINOv2: Learning robust visual features without supervision," *arXiv:2304.07193*, 2023.
- [25] R. Rombach, A. Blattmann, D. Lorenz, P. Esser, and B. Ommer, "High-resolution image synthesis with latent diffusion models," in *CVPR*, 2022.
- [26] L. Tang, M. Jia, Q. Wang, C. P. Phoo, and B. Hariharan, "Emergent correspondence from image diffusion," *NeurIPS*, 2023.
- [27] J. Zhang, C. Herrmann, J. Hur, L. Polania Cabrera, V. Jampani, D. Sun, and M.-H. Yang, "A tale of two features: Stable diffusion complements dino for zero-shot semantic correspondence," *NeurIPS*, 2023.
- [28] X. Li, J. Lu, K. Han, and V. Prisacariu, "Sd4match: Learning to prompt stable diffusion model for semantic matching," *CVPR*, 2024.
- [29] J. Zhang, C. Herrmann, J. Hur, E. Chen, V. Jampani, D. Sun, and M.-H. Yang, "Telling left from right: Identifying geometry-aware semantic correspondence," in *CVPR*, 2024.
- [30] F. Fundel, J. Schusterbauer, V. T. Hu, and B. Ommer, "Distillation of diffusion features for semantic correspondence," in *WACV*, 2025.
- [31] R. Hartley and A. Zisserman, *Multiple view geometry in computer vision*. Cambridge university press, 2003.
- [32] J. Ma, X. Jiang, A. Fan, J. Jiang, and J. Yan, "Image matching from handcrafted to deep features: A survey," *IJCV*, 2021.
- [33] D. Marr and T. Poggio, "A computational theory of human stereo vision," *Proceedings of the Royal Society of London. Series B. Biological Sciences*, 1979.
- [34] B. K. Horn and B. G. Schunck, "Determining optical flow," *Artificial intelligence*, 1981.
- [35] D. G. Lowe, "Distinctive image features from scale-invariant keypoints," *IJCV*, 2004.
- [36] S. Lazebnik, C. Schmid, and J. Ponce, "A maximum entropy framework for part-based texture and object recognition," in *ICCV'05*, 2005.
- [37] A. Kushal, C. Schmid, and J. Ponce, "Flexible object models for category-level 3d object recognition," in *CVPR*, 2007.
- [38] J. Kim, C. Liu, F. Sha, and K. Grauman, "Deformable spatial pyramid matching for fast dense correspondences," in *CVPR*, 2013.
- [39] H. Yang, W.-Y. Lin, and J. Lu, "Daisy filter flow: A generalized discrete approach to dense correspondences," in *CVPR*, 2014.
- [40] E. Tola, V. Lepetit, and P. Fua, "Daisy: An efficient dense descriptor applied to wide-baseline stereo," *TPAMI*, 2010.
- [41] B. Ham, M. Cho, C. Schmid, and J. Ponce, "Proposal flow," in *CVPR*, 2016.
- [42] —, "Proposal flow: Semantic correspondences from object proposals," *TPAMI*, 2018.
- [43] H. Bristow, J. Valmadre, and S. Lucey, "Dense semantic correspondence where every pixel is a classifier," in *ICCV*, 2015.
- [44] J. Hur, H. Lim, C. Park, and S. C. Ahn, "Generalized deformable spatial pyramid: Geometry-preserving dense correspondence estimation," in *CVPR*, 2015.
- [45] B. Ham, M. Cho, C. Schmid, and J. Ponce, "Proposal flow," in *CVPR*, 2016.
- [46] —, "Proposal flow: Semantic correspondences from object proposals," *TPAMI*, 2018.
- [47] T. Taniai, S. N. Sinha, and Y. Sato, "Joint recovery of dense correspondence and cosegmentation in two images," in *CVPR*, 2016.
- [48] F. Yang, X. Li, H. Cheng, J. Li, and L. Chen, "Object-aware dense semantic correspondence," in *CVPR*, 2017.
- [49] O. Duchenne, A. Joulin, and J. Ponce, "A graph-matching kernel for object categorization," in *ICCV*, 2011.
- [50] M. Cho and K. M. Lee, "Progressive graph matching: Making a move of graphs via probabilistic voting," in *CVPR*, 2012.
- [51] C. Choy, J. Gwak, S. Savarese, and M. Chandraker, "Universal correspondence network," in *NeurIPS*, 2016.
- [52] J. L. Long, N. Zhang, and T. Darrell, "Do convnets learn correspondence?" in *NeurIPS*, 2014.
- [53] B. Hariharan, P. Arbeláez, R. Girshick, and J. Malik, "Hypercolumns for object segmentation and fine-grained localization," in *CVPR*, 2015.
- [54] D. Zhao, Z. Song, Z. Ji, G. Zhao, W. Ge, and Y. Yu, "Multi-scale matching networks for semantic correspondence," in *ICCV*, 2021.
- [55] H. Jin and H. Li, "Independently keypoint learning for small object semantic correspondence," *arXiv preprint arXiv:2404.02678*, 2024.
- [56] Y. Sun, Z. Yin, H. Wang, Y. Wang, X. Qiu, W. Ge, and W. Zhang, "Pixel-level semantic correspondence through layout-aware representation learning and multi-scale matching integration," in *CVPR*, 2024.
- [57] G. Luo, L. Dunlap, D. H. Park, A. Holynski, and T. Darrell, "Diffusion hyperfeatures: Searching through time and space for semantic correspondence," *NeurIPS*, 2023.
- [58] X. Li, K. Han, X. Wan, and V. A. Prisacariu, "Simsc: A simple framework for semantic correspondence with temperature learning," *arXiv preprint arXiv:2305.02385*, 2023.
- [59] E. Hedlin, G. Sharma, S. Mahajan, H. Isack, A. Kar, A. Tagliasacchi, and K. M. Yi, "Unsupervised semantic correspondence using stable diffusion," *NeurIPS*, 2024.
- [60] S. Suri, M. Walmer, K. Gupta, and A. Shrivastava, "Lift: A surprisingly simple lightweight feature transform for dense vit descriptors," in *ECCV*, 2024.
- [61] M. Medress, F. Cooper, J. Forgie, C. Green, D. Klatt, M. O'Malley, E. Neuburg, A. Newell, D. Reddy, B. Ritea, J. Shoup-Hummel, D. Walker, and W. Woods, "Speech understanding systems: Report of a steering committee," *Artificial Intelligence*, 1977.
- [62] T.-Y. Lin, P. Dollár, R. Girshick, K. He, B. Hariharan, and S. Belongie, "Feature pyramid networks for object detection," in *CVPR*, 2017.
- [63] R. Gal, Y. Alaluf, Y. Atzmon, O. Patashnik, A. H. Bermano, G. Chechik, and D. Cohen-Or, "An image is worth one word: Personalizing text-to-image generation using textual inversion," *arXiv preprint arXiv:2208.01618*, 2022.
- [64] X. Cheng, C. Deng, A. W. Harley, Y. Zhu, and L. Guibas, "Zero-shot image feature consensus with deep functional maps," in *ECCV*, 2024.
- [65] P. Truong, M. Danelljan, and R. Timofte, "GLU-Net: Global-local universal network for dense flow and correspondences," in *CVPR*, 2020.
- [66] S. Amir, Y. Gandelsman, S. Bagon, and T. Dekel, "Deep vit features as dense visual descriptors," in *ECCVW*, 2022.
- [67] N. Ufer and B. Ommer, "Deep semantic feature matching," in *CVPR*, 2017, pp. 5929–5938.
- [68] S. Hong, S. Cho, S. Kim, and S. Lin, "Integrative feature and cost aggregation with transformers for dense correspondence," *arXiv preprint arXiv:2209.08742*, 2022.
- [69] P. Truong, M. Danelljan, F. Yu, and L. Van Gool, "Warp consistency for unsupervised learning of dense correspondences," in *ICCV*, 2021.
- [70] X. Li, K. Han, S. Li, and V. Prisacariu, "Dualrc: A dual-resolution learning framework with neighbourhood consensus for visual correspondences," *TPAMI*, 2024.
- [71] —, "Dual-resolution correspondence networks," in *NeurIPS*, 2020.
- [72] Y. Sun, D. Zhao, Z. Yin, Y. Huang, T. Gui, W. Zhang, and W. Ge, "Correspondence transformers with asymmetric feature learning and matching flow super-resolution," in *CVPR*, 2023.
- [73] S. Jeon, D. Min, S. Kim, J. Choe, and K. Sohn, "Guided semantic flow," in *ECCV*, 2020.
- [74] J. Kim, K. Ryoo, J. Seo, G. Lee, D. Kim, H. Cho, and S. Kim, "Semi-supervised learning of semantic correspondence with pseudo-labels," in *CVPR*, 2022.
- [75] S. Huang, L. Yang, B. He, S. Zhang, X. He, and A. Shrivastava, "Learning semantic correspondence with sparse annotations," in *ECCV*, 2022.
- [76] S. Kim, D. Min, S. Jeong, S. Kim, S. Jeon, and K. Sohn, "Semantic

- attribute matching networks,” in *CVPR*, 2019.
- [77] A. Thai, W. Wang, H. Tang, S. Stojanov, J. M. Rehg, and M. Feiszli, “3× 2: 3d object part segmentation by 2d semantic correspondences,” in *ECCV*, 2024.
- [78] J. Min, S. Kim, and M. Cho, “Convolutional hough matching networks for robust and efficient visual correspondence,” *TPAMI*, 2023.
- [79] I. Rocco, R. Arandjelović, and J. Sivic, “End-to-end weakly-supervised semantic alignment,” in *CVPR*, 2018.
- [80] S. Kim, D. Min, S. Lin, and K. Sohn, “Dctm: Discrete-continuous transformation matching for semantic flow,” in *ICCV*, 2017.
- [81] J. Bian, W.-Y. Lin, Y. Matsushita, S.-K. Yeung, T.-D. Nguyen, and M.-M. Cheng, “Gms: Grid-based motion statistics for fast, ultra-robust feature correspondence,” in *CVPR*, 2017.
- [82] T. Sattler, B. Leibe, and L. Kobbelt, “Improving ransac’s efficiency with a spatial consistency filter [c],” in *ICCV*, 2009.
- [83] F. Schaffalitzky and A. Zisserman, “Automated scene matching in movies,” in *Image and Video Retrieval: International Conference*, 2002.
- [84] Sivic and Zisserman, “Video google: A text retrieval approach to object matching in videos,” in *ICCV*, 2003.
- [85] M. Bleyer, C. Rhemann, and C. Rother, “Patchmatch stereo-stereo matching with slanted support windows,” in *BMVC*, vol. 11, 2011.
- [86] A. Vaswani, N. Shazeer, N. Parmar, J. Uszkoreit, L. Jones, A. N. Gomez, L. Kaiser, and I. Polosukhin, “Attention is all you need,” *arXiv preprint arXiv:1706.03762*, 2017.
- [87] A. Dosovitskiy, L. Beyer, A. Kolesnikov, D. Weissenborn, X. Zhai, T. Unterthiner, M. Dehghani, M. Minderer, G. Heigold, S. Gelly, J. Uszkoreit, and N. Houlsby, “An image is worth 16x16 words: Transformers for image recognition at scale,” in *ICLR*, 2021.
- [88] N. Carion, F. Massa, G. Synnaeve, N. Usunier, A. Kirillov, and S. Zagoruyko, “End-to-end object detection with transformers,” in *ECCV*, 2020.
- [89] X. Zhu, W. Su, L. Lu, B. Li, X. Wang, and J. Dai, “Deformable detr: Deformable transformers for end-to-end object detection,” *arXiv preprint arXiv:2010.04159*, 2020.
- [90] J. Sun, Z. Shen, Y. Wang, H. Bao, and X. Zhou, “Loftr: Detector-free local feature matching with transformers,” in *CVPR*, 2021.
- [91] S. Hong, S. Cho, J. Nam, S. Lin, and S. Kim, “Cost aggregation with 4D convolutional swin transformer for few-shot segmentation,” in *ECCV*, 2022.
- [92] Z. Liu, Y. Lin, Y. Cao, H. Hu, Y. Wei, Z. Zhang, S. Lin, and B. Guo, “Swin transformer: Hierarchical vision transformer using shifted windows,” in *ICCV*, 2021.
- [93] S. Hong, J. Nam, S. Cho, S. Hong, S. Jeon, D. Min, and S. Kim, “Neural matching fields: Implicit representation of matching fields for visual correspondence,” *NeurIPS*, 2022.
- [94] I. Rocco, R. Arandjelovic, and J. Sivic, “Convolutional neural network architecture for geometric matching,” in *CVPR*, 2017.
- [95] P. H. Seo, J. Lee, D. Jung, B. Han, and M. Cho, “Attentive semantic alignment with offset-aware correlation kernels,” in *ECCV*, 2018.
- [96] S. Kim, S. Lin, S. Jeon, D. Min, and K. Sohn, “Recurrent transformer networks for semantic correspondence,” in *NeurIPS*, 2018.
- [97] S. Jeon, S. Kim, D. Min, and K. Sohn, “Parn: Pyramidal affine regression networks for dense semantic correspondence,” in *ECCV*, 2018.
- [98] I. Rocco, R. Arandjelović, and J. Sivic, “Efficient neighbourhood consensus networks via submanifold sparse convolutions,” in *ECCV*, 2020.
- [99] J. Edstedt, I. Athanasiadis, M. Wadenbäck, and M. Felsberg, “Dkm: Dense kernelized feature matching for geometry estimation,” in *CVPR*, 2023.
- [100] Y. Huang, Y. Sun, C. Lai, Q. Xu, X. Wang, X. Shen, and W. Ge, “Weakly supervised learning of semantic correspondence through cascaded online correspondence refinement,” in *ICCV*, 2023.
- [101] J. Deng, W. Dong, R. Socher, L.-J. Li, K. Li, and L. Fei-Fei, “Imagenet: A large-scale hierarchical image database,” in *CVPR*, 2009.
- [102] T. Zhou, Y. Jae Lee, S. X. Yu, and A. A. Efros, “FlowWeb: Joint image set alignment by weaving consistent, pixel-wise correspondences,” in *CVPR*, 2015.
- [103] Z. Laskar, H. R. Tavakoli, and J. Kannala, “Semantic matching by weakly supervised 2d point set registration,” *arXiv preprint arXiv:1901.08341*, 2019.
- [104] Y.-C. Chen, P.-H. Huang, L.-Y. Yu, J.-B. Huang, M.-H. Yang, and Y.-Y. Lin, “Deep semantic matching with foreground detection and cycle-consistency,” in *ACCV*, 2018.
- [105] A. Shtedritski, A. Vedaldi, and C. Rupprecht, “Learning universal semantic correspondences with no supervision and automatic data curation,” 2023.
- [106] P. Truong, M. Danelljan, F. Yu, and L. Van Gool, “Probabilistic warp consistency for weakly-supervised semantic correspondences,” in *CVPR*, 2022.
- [107] T. Zhou, P. Krahenbuhl, M. Aubry, Q. Huang, and A. A. Efros, “Learning dense correspondence via 3d-guided cycle consistency,” in *CVPR*, 2016.
- [108] J.-Y. Zhu, T. Park, P. Isola, and A. A. Efros, “Unpaired image-to-image translation using cycle-consistent adversarial networks,” in *ECCV*, 2017.
- [109] X. Li, D.-P. Fan, F. Yang, A. Luo, H. Cheng, and Z. Liu, “Probabilistic model distillation for semantic correspondence,” in *CVPR*, 2021.
- [110] B. Han, Q. Yao, X. Yu, G. Niu, M. Xu, W. Hu, I. Tsang, and M. Sugiyama, “Co-teaching: Robust training of deep neural networks with extremely noisy labels,” *NIPS*, 2018.
- [111] J. Kim, B. Heo, S. Yun, S. Kim, and D. Han, “Match me if you can: Semantic correspondence learning with unpaired images,” *arXiv preprint arXiv:2311.18540*, 2023.
- [112] L. Fei-Fei, R. Fergus, and P. Perona, “Learning generative visual models from few training examples: An incremental bayesian approach tested on 101 object categories,” in *CVPRW*, 2004.
- [113] F.-F. Li, R. Fergus, and P. Perona, “One-shot learning of object categories,” *TPAMI*, 2006.
- [114] X. Chen, R. Mottaghi, X. Liu, S. Fidler, R. Urtasun, and A. Yuille, “Detect what you can: Detecting and representing objects using holistic models and body parts,” in *CVPR*, 2014.
- [115] T. Tanai, S. N. Sinha, and Y. Sato, “Joint recovery of dense correspondence and cosegmentation in two images,” in *CVPR*, 2016.
- [116] Y.-L. Lin, V. I. Morariu, W. Hsu, and L. S. Davis, “Jointly optimizing 3D model fitting and fine-grained classification,” in *ECCV*, 2014.
- [117] M. Rubinstein, A. Joulin, J. Kopf, and C. Liu, “Unsupervised joint object discovery and segmentation in internet images,” in *CVPR*, 2013.
- [118] B. Hariharan, P. Arbeláez, L. Bourdev, S. Maji, and J. Malik, “Semantic contours from inverse detectors,” in *ICCV*, 2011.
- [119] M. Everingham, S. M. A. Eslami, L. Van Gool, C. K. I. Williams, J. Winn, and A. Zisserman, “The pascal visual object classes challenge: A retrospective,” *IJCV*, 2015.
- [120] G. Griffin, A. Holub, and P. Perona, “Caltech-256 object category dataset,” *CalTech Report*, 2007.
- [121] M. Cho, K. Alahari, and J. Ponce, “Learning graphs to match,” in *ICCV*, 2013.
- [122] J. Min, J. Lee, J. Ponce, and M. Cho, “SPair-71k: A large-scale benchmark for semantic correspondence,” *arXiv preprint arXiv:1908.10543*, 2019.
- [123] Y. Xiang, R. Mottaghi, and S. Savarese, “Beyond pascal: A benchmark for 3d object detection in the wild,” *WACV*, 2014.
- [124] H. Yu, Y. Xu, J. Zhang, W. Zhao, Z. Guan, and D. Tao, “Ap-10k: A benchmark for animal pose estimation in the wild,” in *NeurIPS*, 2021.
- [125] Y. Xian, C. H. Lampert, B. Schiele, and Z. Akata, “Zero-shot learning—a comprehensive evaluation of the good, the bad and the ugly,” *TPAMI*, 2018.
- [126] B. Ferreira, “African wildlife,” <https://www.kaggle.com/biancaferreira/african-wildlife>, 2021.
- [127] E. Šahović, “wild cats,” <https://www.kaggle.com/enisahovi/cats-projekat-4>, 2020.
- [128] Y. V. Trivedi, “Animals 5,” <https://www.kaggle.com/ytrivedi/animals-5>, 2020.
- [129] A. Saxena, “Animal image dataset(dog, cat and panda),” <https://www.kaggle.com/ashishsaxena2209/animal-image-datasetdog-cat-and-panda>, 2019.
- [130] C. Alessio, “Animals 10,” <https://www.kaggle.com/alessiocorrado99/animals10>, 2019.
- [131] antoreepjana, “Iucn animals dataset,” <https://www.kaggle.com/antoreepjana/iucn-animals-dataset>, 2021.
- [132] S. Jamil, “Endangered animals,” <https://www.kaggle.com/sonain/endangered-animals>, 2020.
- [133] Y. Sun, Y. Huang, H. Guo, Y. Zhao, R. Wu, Y. Yu, W. Ge, and W. Zhang, “Misc210k: A large-scale dataset for multi-instance semantic correspondence,” in *CVPR*, 2023.
- [134] S. Cho, S. Hong, S. Jeon, Y. Lee, K. Sohn, and S. Kim, “Semantic correspondence with transformers,” *arXiv preprint arXiv:2106.02520*, 2021.
- [135] M. Caron, H. Touvron, I. Misra, H. Jégou, J. Mairal, P. Bojanowski, and A. Joulin, “Emerging properties in self-supervised vision transformers,” in *ICCV*, 2021.
- [136] M. Aygün and O. Mac Aodha, “Demystifying unsupervised semantic correspondence estimation,” in *ECCV*, 2022.
- [137] K. Gupta, V. Jampani, C. Esteves, A. Shrivastava, A. Makadia,

- N. Snaveley, and A. Kar, "Asic: Aligning sparse in-the-wild image collections," in *ICCV*, 2023.
- [138] Y. Liu, L. Zhu, M. Yamada, and Y. Yang, "Semantic correspondence as an optimal transport problem," in *CVPR*, 2020.
- [139] K. He, X. Zhang, S. Ren, and J. Sun, "Deep residual learning for image recognition," in *CVPR*, 2016.
- [140] A. Radford, J. W. Kim, C. Hallacy, A. Ramesh, G. Goh, S. Agarwal, G. Sastry, A. Askell, P. Mishkin, J. Clark *et al.*, "Learning transferable visual models from natural language supervision," in *ICML*, 2021.
- [141] J. Zhou, C. Wei, H. Wang, W. Shen, C. Xie, A. Yuille, and T. Kong, "ibot: Image bert pre-training with online tokenizer," *ICLR*, 2022.

**Overview.** In this appendix, we present detailed experimental evaluations and qualitative analysis to support our main findings. In Section A, we evaluate feature enhancement modules by comparing CNN and Transformer approaches (Section A-A) and assess several cost aggregation methods including Neighbourhood Consensus, CATs Aggregator, and Match-to-Match attention module (Section A-B). Section B shows our qualitative analysis, where we demonstrate our method’s robustness compared to state-of-the-art approach GeoAware-SC [29].

## APPENDIX A

### FEATURE ENHANCEMENT AND MATCHING REFINEMENT EVALUATION

This section provides experimental details described in Section VI-B and Section VI-C, conducted across different resolutions.

#### A. Feature Enhancement Evaluation

We compare the performance of CNN and Transformer feature enhancement modules across different resolutions, experimental results are provided in Table A1.

All feature enhancement methods generally improve the performance compared to the baseline (no feature enhancement) across different resolutions. The improvements are more significant in the frozen backbone setting compared to the fine-tuned setting.

#### B. Cost Aggregation Evaluation

We compare the performance of the Neighbourhood Consensus, CATs Aggregator, and Match-to-Match attention module. The detailed evaluation results are provided in Table A2. Due to the computational cost of high-resolution inputs, the original Neighbourhood Consensus setting is applied only at the 224 resolution. For the 448 and 840 resolutions, we use three layers of  $3 \times 3 \times 3 \times 3$  filters while reducing the number of intermediate channels to half of the original configuration.

The experimental results demonstrate that NeighConsensus consistently outperforms other cost aggregators across different resolutions, and the original implementation of NeighConsensus (Ori.) also shows competitive performance, especially at lower resolutions.

## APPENDIX B

### QUALITATIVE ANALYSIS

Compared to state-of-the-art method GeoAware-SC [29], our proposed baseline demonstrates superior robustness across a wide range of real-world scenarios. As shown in Figure B1, we visualize the matching results on a wide range of categories including animals (horses, dogs, birds), vehicles (motorcycles, buses, aircraft), and everyday objects. The method successfully handles challenging cases with dramatic changes in viewpoint, illumination, and appearance variations. Particularly noteworthy is its ability to establish reliable correspondences despite significant geometric deformations, such as in the cases of moving animals and vehicles captured from different angles.

TABLE A1

EVALUATION OF DIFFERENT BOTTLENECKS ON THE SPAIR-71k DATASET. THE METHODS ARE CATEGORIZED INTO TWO TYPES: FROZEN DINOv2 BACKBONE AND JOINT TRAINING OF THE LAST LAYER OF DINOv2 AND BOTTLENECK. THE HIGHEST PCK VALUES ARE HIGHLIGHTED IN BOLD, WHILE BASELINE METHODS (WITHOUT BOTTLENECK) ARE INDICATED IN GRAY. FT.: FINE-TUNE, RESO.: IMAGE RESOLUTION, FEATURE MAP SIZE.

Backbone	FT.	Bottleneck	Reso.	SPair-71k					$\Delta PCK_{\alpha 0.1}$
				PCK @ $\alpha_{\text{bbox}}$					
				0.01	0.05	0.1	0.15		
DINOv2	×	-	840, 60	7.3	40.0	54.4	62.8	-	
DINOv2	×	ResNet Bottleneck Block	840, 60	10.3	60.2	75.2	81.3	+20.8	
DINOv2	×	Self-Attention	840, 60	11.8	60.8	<b>76.5</b>	83.1	+22.1	
DINOv2	×	Self+Cross Attention	840, 60	11.5	60.6	<u>76.3</u>	83.2	+21.9	
DINOv2	×	-	448, 32	3.7	35.4	52.9	62.2	-	
DINOv2	×	ResNet Bottleneck Block	448, 32	4.3	46.9	69.5	78.7	+16.6	
DINOv2	×	Self-Attention	448, 32	5.3	49.2	70.2	78.7	+17.3	
DINOv2	×	Self+Cross Attention	448, 32	5.7	49.6	69.8	78.3	+16.9	
DINOv2	×	-	224, 16	1.1	20.9	43.1	56.2	-	
DINOv2	×	ResNet Bottleneck Block	224, 16	1.3	23.8	50.9	66.3	+7.8	
DINOv2	×	Self-Attention	224, 16	1.1	20.5	44.8	59.6	+1.7	
DINOv2	×	Self+Cross Attention	224, 16	1.6	25.3	50.2	63.8	+7.1	
DINOv2	✓	-	840, 60	15.0	67.4	<u>81.7</u>	87.1	-	
DINOv2	✓	ResNet Bottleneck Block	840, 60	15.1	71.1	<b>84.2</b>	88.9	+2.5	
DINOv2	✓	Self-Attention	840, 60	13.9	66.4	80.9	87.1	-0.8	
DINOv2	✓	Self+Cross Attention	840, 60	14.5	66.3	80.9	87.0	-0.8	
DINOv2	✓	-	448, 32	7.1	56.2	76.6	84.3	-	
DINOv2	✓	ResNet Bottleneck Block	448, 32	6.3	57.9	79.8	86.8	+3.2	
DINOv2	✓	Self-Attention	448, 32	7.6	57.2	77.2	85.1	+0.6	
DINOv2	✓	Self+Cross Attention	448, 32	7.8	58.2	78.4	86.0	+1.8	
DINOv2	✓	-	224, 16	1.9	30.5	58.2	72.1	-	
DINOv2	✓	ResNet Bottleneck Block	224, 16	1.7	29.8	60.4	75.2	+2.2	
DINOv2	✓	Self-Attention	224, 16	2.1	32.0	60.8	74.6	+2.6	
DINOv2	✓	Self+Cross Attention	224, 16	2.2	33.0	61.0	74.5	+2.8	

TABLE A2  
 EVALUATION OF NEIGHBOURHOOD CONSENSUS MODULE ON THE SPAIR-71K DATASET. FT.: FINE-TUNE. THE METHODS ARE CATEGORIZED INTO TWO TYPES: FROZEN DINOv2 BACKBONE AND JOINT TRAINING OF THE LAST LAYER OF DINOv2 AND THE COST AGGREGATOR. THE BASELINE METHODS ARE INDICATED IN GRAY. NEIGHCONSENSUS (ORI.) DENOTES THE ORIGINAL IMPLEMENTATION OF NEIGHCONSENSUS IN NC-NET [17].

Backbone	FT.	Cost Aggregator	Reso.	SPair-71k				
				PCK @ $\alpha_{\text{bbox}}$				$\Delta\text{PCK}_{\alpha 0.1}$
				0.01	0.05	0.1	0.15	
DINOv2	×	-	840, 60	7.3	40.0	<u>54.4</u>	62.8	-
DINOv2	×	Match2Match	840, 60	6.8	39.5	54.1	62.6	-0.3
DINOv2	×	NeighConsensus	840, 60	6.2	45.8	<b>61.9</b>	69.3	+7.5
DINOv2	×	-	448, 32	3.7	35.4	<u>52.9</u>	62.2	-
DINOv2	×	CATs	448, 32	2.6	30.8	49.5	59.7	-3.4
DINOv2	×	Match2Match	448, 32	3.6	34.8	52.2	61.7	-0.7
DINOv2	×	NeighConsensus	448, 32	2.8	33.4	<b>56.5</b>	67.7	+3.6
DINOv2	×	-	224, 16	1.1	20.9	43.1	56.2	-
DINOv2	×	CATs	224, 16	1.0	18.4	40.2	53.4	-2.9
DINOv2	×	Match2Match	224, 16	1.1	20.8	42.9	55.4	-0.2
DINOv2	×	NeighConsensus	224, 16	0.9	18.0	<u>43.4</u>	60.5	+0.3
DINOv2	×	NeighConsensus (Ori.)	224, 16	1.1	20.4	<b>47.1</b>	63.3	+4.0
DINOv2	✓	-	840, 60	15.0	67.4	<u>81.7</u>	87.1	-
DINOv2	✓	Match2Match	840, 60	13.9	68.3	<u>83.3</u>	88.6	+1.6
DINOv2	✓	NeighConsensus	840, 60	12.7	70.2	<b>85.2</b>	89.6	+3.5
DINOv2	✓	-	448, 32	7.1	56.2	76.6	84.3	-
DINOv2	✓	CATs	448, 32	3.2	42.6	71.4	82.4	-5.2
DINOv2	✓	Match2Match	448, 32	6.3	55.4	<u>77.8</u>	85.9	+1.2
DINOv2	✓	NeighConsensus	448, 32	5.0	54.7	<b>79.4</b>	87.3	+2.8
DINOv2	✓	-	224, 16	1.9	30.5	58.2	72.1	-
DINOv2	✓	CATs	224, 16	1.3	23.1	52.1	68.8	-6.1
DINOv2	✓	Match2Match	224, 16	1.8	30.7	59.8	73.9	+1.6
DINOv2	✓	NeighConsensus	224, 16	1.9	31.5	<u>62.4</u>	77.1	+4.2
DINOv2	✓	NeighConsensus (Ori.)	224, 16	2.5	36.4	<b>66.1</b>	79.2	+7.9



Fig. B1. Visualization of feature matching results across diverse scenarios. Our proposed baseline successfully handles significant appearance variations and geometric deformations while maintaining reliable correspondences across various object categories.